Energetics of oxidation and formation of uranium mononitride

Vitaliy G. Goncharov[1,2,3,4], Juejing Liu[1,2,3], Kyle Kriegsman[1,2,3], Chris Benmore[5], Chengjun Sun[5], Shelly Kelly[5], Joshua T. White[6], Hongwu Xu[4,7*], and Xiaofeng Guo[1,2,3*]

[1] *Department of Chemistry, Washington State University, Pullman, Washington 99164, United States*

[2] *Alexandra Navrotsky Institute for Experimental Thermodynamics, Washington State University, Pullman, Washington 99164, United States*

[3] *Materials Science and Engineering Program, Washington State University, Pullman, Washington 99164, United States*

[4]*Earth and Environmental Science Division, Los Alamos National Laboratory, Los Alamos, New Mexico, 87545, United States*

[5] *X-ray Science Division, Argonne National Laboratory, 9700 South Cass Avenue, Argonne, Illinois, 60439, United States*

[6] *Materials Science and Technology Division, Los Alamos National Laboratory, Los Alamos, New Mexico 87545, United States*

[7] *School of Molecular Sciences and Center for Materials of the Universe, Arizona State University, Tempe, Arizona, 85287, United States*

---

* e-mails of corresponding authors: hxu@lanl.gov; x.guo@wsu.edu

Submitting to Journal of Nuclear Materials

Abstract

Uranium mononitride (UN) is an advanced nuclear fuel currently being considered for use in several generation IV fast and thermal neutron spectrum core designs, with additional applications to thermal and electric nuclear propulsion reactors. To better understand the thermal behavior and thermodynamic stability of UN, we investigated the bulk thermal oxidation process and thermochemical reactions, including the enthalpy of oxidation and standard enthalpy of formation, by conducting thermalgravimetric analysis – differential scanning calorimetry coupled with mass spectrometry (TGA-DSC-MS), and high temperature transposed temperature drop and oxide melt drop solution calorimetry. The bulk oxidation of UN (containing a small amount of α-$UN_{1.5+x}$) in air was found to follow a step-wise process characterized by consecutive oxidative reactions UN-$UN_{1.5+x}$-UO_2 → UO_2-UO_3-N_k → UO_3-N_k → UO_3 → U_3O_8. TGA results support that the UO_2 – U_2N_{3+x} passivating layer (previously hypothesized in the literature) delays the onset of rapid bulk oxidation of UN in air up to 389 °C. *Ex situ* synchrotron X-ray diffraction and X-ray absorption fine structure (XAFS) analyses were performed to characterize UN and its final oxidized product. The standard enthalpy of formation ($\Delta H°_f$) of UN was determined to be –144.4 ± 5.9 kJ/mol·atom, in good agreement with previously determined enthalpies of formation of UN from Pt encapsulation and bomb calorimetric experiments. We also report a negative linear correlation between $\Delta H°_f$ and the N/U molar ratio, based on the thermochemical data obtained in this work and those previously reported for β-$UN_{1.5-x}$ and α-$UN_{1.5+x}$. Results obtained in this work thus shed light on certain thermal and thermodynamic issues associated with utilization of UN as a nuclear fuel in generation IV and propulsion nuclear reactors.

Keywords: uranium nitride, thermal oxidation, standard enthalpy of formation, passivating layer, high temperature calorimetry

Highlights:

- UN exhibits step-wise oxidation behavior in air
- UN forms a protective passivating layer preventing its rapid bulk oxidation up to 389 ºC
- Standard enthalpy of formation of UN was determined by high temperature solution and transposed temperature drop calorimetry at 700 ºC

- Standard enthalpies of formation of UN, β-$UN_{1.5-x,}$ and α-$UN_{1.5+x}$ system possess a negative linear correlation with the N/U molar ratio.

1. Introduction

In recent years, advanced ceramic nuclear fuels (e.g., UN, UC, U_3Si_2) have received a considerable renewed research interest owing to their superior thermophysical properties when compared to traditional oxide-based (UO_2) fuels.[1–11] In particular, uranium mononitride (UN) has been proposed as an accident tolerant fuel (ATF), due to its high uranium density (34.2 U atom/nm^3 and 24.5 U atom/nm^3 for UN and UO_2 respectively),[12] excellent thermal conductivity at high temperatures (4.0 W/m·°C and 2.2 W/m·°C for UN and UO_2 respectively at 200 °C and 20.0 W/m·°C versus 3.4 W/m·°C for UN and UO_2 at 1000 °C respectively),[3] ~20 % reduced swelling rate and a ~55 % lower release of fission gasses when normalized to the swelling rate and fission gas release of UO_2.[3,13–18] In addition, many fission products and higher actinides form stable nitride phases and may be incorporated into the UN matrix to form multi-component solid solutions,[19,20] extending the fuel's operational life-span and stability within the reactor. Another advantage of UN arises from its chemical versatility,[19–22] which makes the fuel readily compatible with present cladding materials (such as Zr and Ni alloys), or liquid metal Na or Pb coolants. When enriched with ^{15}N, UN possesses excellent neutron economy enabling operations in both, thermal and fast neutron reactor regimes through mitigation of the unfavorable $N^{14}(n, p)C^{14}$ and $N^{14}(n, \alpha)B^{11}$ neutronic side reactions,[23] allowing UN to be an effective fuel for various reactor designs. [18,20,21]

Accordingly, UN promises to be an excellent fuel candidate for a number of Generation IV (Gen IV) advanced reactors such as sodium-cooled (SFR),[24,25] lead-cooled (LFR)[26] fast reactors,[27–31], and gas (He) cooled very-high temperature reactors (VHTR) [32]. Additionally, UN is being considered as the fissile component in several CERMET fuel (fissile An-containing ceramic particles embedded in a refractory metal structural matrix, e.g., W/UN and Mo/UN) designs to be used in nuclear thermal propulsion (NTP) rockets for accelerated manned missions to Mars.[33–35] Thus, there has been continued interest in tuning the chemistry and structures of novel U-based ceramic compounds for use in various advanced reactor designs.[36–38]

However, a major drawback in using UN as the primary fuel component for Gen IV or NTP reactors is the limited thermophysical data describing the thermal and thermodynamic aspects of UNs stability in various environments.[39,40] Important thermochemical properties include thermal oxidation behavior, enthalpies of oxidation, and enthalpies of formation. Although thermodynamic properties of the uranium nitride systems such as standard enthalpies of formations

have been previously measured,[2,41–45] ambiguity remains due to their thermal oxidation behavior and related non-stoichiometric thermochemistry. There have been two primary challenges when examining the thermodynamic behavior of UN. First, the possibility of having an incomplete combustion leading to phase uncertainty of the final product in a bomb calorimeter may lead to inaccuracies in determination of the standard enthalpy of formation of UN. The second challenge arises from the susceptibility of U to form uranium oxynitride layer (UN_xO_y) on the surface of UN upon its exposure to oxygen, which can further disproportionate into UO_2 and U_2N_{3+x} during extended exposure or at temperatures > 200 °C.[46] Dell *et al.* proposed that such oxidation leads to the formation of a UO_2 – U_2N_{3+x} – UN "sandwich" structure.[46] Although the formation of passivating layer is widely accepted,[46–48] little has been discussed about its implication for mitigation of the onset of bulk oxidation of underlying UN.

In this work, we aim at developing new calorimetric methodology and obtaining new results on the thermochemistry of UN, addressing both challenges. Specifically, thermogravimetric analysis and differential scanning calorimetry coupled with mass spectrometry (TGA-DSC-MS) was conducted to characterize the thermal oxidation behavior of UN in air from room temperature (RT) to 900 ºC. Two types of high temperature drop calorimetry under O_2 environment, namely transposed temperature drop calorimetry and oxide melt drop calorimetry using molten sodium molybdate ($3Na_2O{\cdot}4MoO_3$) solvent, were performed to determine the standard enthalpy of formation (ΔH^o_f) of UN. Such calorimetric methodology was adopted from previous calorimetric work on U-Si systems.[49,50] By using the newly obtained ΔH^o_f(UN), we examined the enthalpies of oxidation of UN to UO_3 and U_3O_8 at ambient conditions, which provide new thermodynamic benchmarks for phase equilibrium modeling and thermodynamic stability. Lastly, we further established an energetic trend of U-N system with the N/U molar ratio ranging from 1.0 to 1.5+x by combining previously determined ΔH^o_f of α-U_2N_{3+x} and β-U_2N_{3-x} phases.[51,52] The results presented in this work can further our understanding of the thermodynamics of UN and advance its applications in future nuclear reactors.

2. Methods

2.1 Sample synthesis

Uranium mononitride samples were prepared using the carbothermic reduction and nitridation of UO_2.[53] Graphite and UO_2 were mixed in appropriate ratios and heated under vacuum in a W-

mesh element furnace to reduce the oxide to a carbide with oxygen impurities. Further heat treatments under N_2 and 5% H_2/N_2 converts the carbide to uranium mononitride powder and further purifies the carbon and oxygen impurities from the nitride. Pellets were prepared from the UN powder by milling in a Si_3N_4 jar followed by sieving with a 325 mesh sieve. The sieved powders were then pressed using a 5.84mm punch and die set to 150 MPa and sintered under Ar at 1800 °C for 8h, which yielded pellets ~89% of the theoretical density of UN. All processing, including the furnace, was conducted in an inert glove box line maintained below 20ppm O. Impurities of the UN pellets were determined using inert gas fusion technique and combustion infrared detection to determine the oxygen and carbon content, respectively. Oxygen and carbon impurities of the pellets were 300 wppm ± 60 wppm, 3500 wppm ± 200 wppm, respectively.

2.2 X-ray diffraction (XRD)

The phase purity of synthesized UN, and phase identification of the oxidized post-calorimetric samples were determined by XRD. We used both lab-based Bruker D2 Phaser X-ray diffractometer (Bruker, WS, USA) and synchrotron XRD at sector 6-ID-D of the Advanced Photon Source (APS) at Argonne National Laboratory (ANL). An approximate 100 mg sample of UN (pristine starting material) was prepared into powder (from as-prepared UN ingot) in an inert Ar atmosphere glovebox. In the lab-XRD measurement, UN oxidized powder was fixed with vacuum grease to an acrylate-domed holder, which provided an inert atmosphere during the XRD measurement sequence. An air scatter shield was equipped on the acrylate dome to minimize its background signal. Measurements were collected with a 0.01° scan step and a dwell time of 4 s per interval. In the synchrotron XRD measurements, UN powder was sealed inside a triple-layer Kapton tube. All collected two-dimensional (2D) images were calibrated, masked, and integrated through the use of Dioptas processing software.[54] The data were analyzed by the Rietveld method using General Structure Analysis System software version II (GSAS-II),[55] where the instrument parameters were obtained using the CeO_2 standard. The backgrounds were modeled by the Chebyshev function with 6 coefficients. The above Rietveld refinement procedures are also stated previously elsewhere.[56–59] Analysis of the post calorimetric sample was conducted in a similar manner. Collected diffraction patterns were analyzed utilizing DIFFRAC.SUITE EVA software package with the ICDD PDF-4+ database. ~15 mg of U_3O_8 obtained from oxidized UN

(recovered from transposed temperature drop calorimetric experiments) was analyzed by a similar method.

2.3 X-ray absorption fine structure (XAFS)

The local structures and phase identities of UN and oxidized powder samples were also studied by XAFS (Figure 2), performed at the sector 20-BM of the APS at ANL. Both samples were finely grounded and mixed with boron nitride to prepare pallets inside an inert N_2 atmosphere glovebox, then sealed inside a double-layer Kapton sample holder. The XAFS spectra were collected from 16965 eV to 18665 eV in transmission mode at room temperature. Each sample was scanned multiple times to improve the data quality. Athena and Artemis software were utilized to process and fit all EXAFS spectra.[60] The energy space spectra were preprocessed and converted to K space (see Figure S1 in SI). The K range for generating real space (*R* space) spectra was from about 3 $Å^{-1}$ to 12 $Å^{-1}$. Theoretical UN and α-U_3O_8 crystal structures were obtained from previous studies.[61,62] *Feff 6 code* was adopted to generate theoretical scatterings from these structures.[63] In the α-U_3O_8 structure, U atoms occupy two different sites.[61,63] The local environments of these two U sites are slightly different resulting in many U-O paths with small coordination numbers (CN) and small distance differences. To simplify the fitting process, we used the aggregation function in Artemis software to generate theoretical U-O paths.[64] This function aggregated U-O paths with similar distances and generated averaged U-O scattering path lengths. The fitting range was 1 Å to 4 Å in the *R* space. The R-factor for two fittings was smaller than 0.02.

2.4 Thermogravimetric analysis – Differential scanning calorimetry (TGA-DSC)

Powdered UN sample (~3.5mg) was loaded into 1 mL alumina crucibles in an inert N_2 glove box. The sealed crucibles were placed in a custom-built air-tight transfer carrier (Figure S2b in the supporting information, SI) and sealed in the glovebox. The carrier was then used to transfer the loaded crucibles to the TGA-DSC instrument (Setaram SetSYS-2400) to minimize the exposure of samples to air. Three types of TGA-DSC experiments were preformed: *i*) a 12-hour isothermal hold of UN at 27 °C in flowing synthetic air (60 ml/min), *ii*) a thermal oxidation of UN from 25 ºC to 900 ºC with a heating rate of 10 ºC/min in flowing synthetic air (60 ml/min), and *iii*) a 5 hour isothermal hold of U_3O_8 (sample recovered from oxidized UN from high temperature transposed

drop calorimetry experiments) at 750 °C in flowing synthetic air (60 ml/min). The sensitivity of the TGA-DSC system was calibrated using the thermal decomposition of CaC_2O_4 and melting cycles of various metals, full description of which may be found elsewhere [65,66]. A summary of the experimental mass changes and the molar stoichiometries of the calculated phases corresponding to thermal oxidation of UN to 900 °C is presented in Table 1.

2.5 Evolved Gas Mass Spectrometry

The gases produced during UN oxidation were analyzed by the Discovery MS (TA Instruments) benchtop quadrupole mass spectrometer optimized for evolved gas analysis. The mass spectrometer was attached to a Q600 SDT (TA Instruments) TGA-DSC instrument. UN samples were loaded into Q600 SDT and heated at a heating rate of 10 ºC/min from 25 to 900 ºC in a flowing synthetic air (60 ml/min, same as the thermal oxidative conditions of the TGA-DSC runs described above). The evolved gas was analyzed using high energy electrons (18 eV) and a Faraday detector system. The TGA-DSC results agree qualitatively with those produced by SetSYS-2400, and thus the MS data was combined with the thermal analyses conducted in SetSYS-2400. The TGA-DSC curve produced by Q600 SDT is presented in Figure S3. The primary MS signals of $m/z = 28$ (N_2) and $m/z = 16$ (O_2), were deconvoluted and presented in Figure S4 and S5 respectively. Likewise, the minor signals of $m/z = 44$ (NO_2) and $m/z = 30$ (NO) are presented in Figure S6. The evolved N_2 and consumed O_2 MS signals are plotted against the SetSYS TGA-DSC curves in Figures 3 and 4, respectively, and their molar (%) values are summarized in Table 2.

2.6 High temperature transposed temperature drop and oxide melt drop solution calorimetry

High temperature calorimetric measurements were conducted using a Tian-Calvet twin microcalorimeter, Setaram Alexsys-1000.[67,68] UN fragments (~ 3 mg) were loaded into capped custom-built steel dropper scoops (Figure S2a), which were then sealed into an air-tight transfer carrier (Figure S2b) under an inert N_2 atmosphere to protect the UN pellet from reacting with oxygen during transfer from the glovebox to the calorimeter. The exposure time of UN pellets to the ambient air was <10 seconds between opening the carrier and performing the calorimetric drop. Each UN pellet was dropped from RT into the calorimeter chamber maintained at 700 ºC where quartz crucibles contained ~15 g molten sodium molybdate solvent ($3NaO{\cdot}4MoO_3$) for the oxide melt drop calorimetry, or no solvent for the transposed temperature drop calorimetry. In both cases,

O_2 gas was continuously flushed through the calorimeter chamber at ~140 mL/min to maintain a constant oxidizing environment and a stable head space above the solvent. In addition, O_2 gas was continuously bubbled through the solvent (for experiments using the oxide melt) at a rate of 20 ml/min to assist sample dissolution and oxidation. The complete dissolution of nitrides and uranium containing compounds has been previously confirmed in molten sodium molybdate solvent.[49,69–76] The calibration, methodology, and U handling employed in the high temperature calorimetric measurements were also described in detail in previous works and have been successfully applied to U-Si intermetallic compounds.[49,50,68,77] The standard enthalpy of formation of UN was calculated by constructing two thermochemical cycles (Tables 3 and 4), which are based on *i*) different reactions UN underwent in the calorimeter chambers when performing the two types of calorimetric experiments described above and *ii*) their corresponding experimentally measured enthalpies of transposed temperature drop (ΔH_{td}) and drop solution (ΔH_{ds}), shown in Tables 3 and 4, respectively.

3. Results and Discussion

3.1 XRD and XAFS characterization of as synthesized UN

Synchrotron XRD pattern of pristine as synthesized UN is presented in Figure 1. According to our results the UN sample is largely phase pure (space group $Fm\bar{3}m$) with a minor presence of secondary α-$UN_{1.5+x}$ (space group $Ia\bar{3}$) [78]. The refined unit cell parameter was determined as a = 4.897(1) Å and is in good agreement with previous UN studies (4.889 Å [79] and 4.907 Å [80]). The secondary α-$UN_{1.5+x}$ may have formed on the UN powders from a disproportionation reaction of UN with access N supplied either by adsorbed N_2 species on the UN surface [81], or by access N included during synthesis [79,80]. Comparison of the XRD pattern of pristine UN to that of UN exposed to the ambient environment for 12 hours (Figure 6) demonstrates increased formation of α-$UN_{1.5+x}$ and β-$UN_{1.5-x}$ phases with prolonged exposure time. This in turn suggests that the formation of these secondary phases likely occurs on the UN surface and is promoted by the interactions of UN with oxygen.[46,47,78] However, the absence of UO_2 diffraction peaks in this sample suggests that oxygen species present on the UN surface are likely poorly crystalline UO_2 or UN_xO_y.[46,47] From the XRD analysis we conclude that the UN samples used for further calorimetric studies are nearly phase pure UN with slight α-$UN_{1.5+x}$ and possible UO_2

contaminations and thus have the chemical formulas in the form of $UN{\cdot}UN_{1.5+x}{\cdot}UO_2$ with $UN >> UN_{1.5+x} > UO_2$.

X-ray absorption fine structure was performed to characterize the local environment of U. The radial distribution function (RDF) of UN (Figure 2a) were retrieved from the Fourier transform of K space spectrum (Figure S1). In the UN RDF spectrum, the U-N 1st path peak (at ~2.0 Å) splits into two peaks with similar amplitudes, which implies a distortion in the first coordination shell of U. Detailed XAFS fitting (Figures 1b and 1c) using the rock salt structure (space group $Fm\bar{3}m$, Figure 2c) further confirms the distortion (Table S1) from a theoretical 6-coordinated U (with a U-N bond length of 2.44 Å) to 2.9-coordinated U (with a U-N bond length of 2.36 Å) and 2.4-coordinated U (with a U-N bond length of 2.44 Å). The U-U 1st path scattering contributes to the large peak located at about 3.2 Å, although it was fitted with only 7.3 U atoms instead of 12. Besides reasons such as large Debye-Waller factors, missing atoms in U-U path may also be due to destructive scattering interference when many sub-shells are formed with small distance differences so that some atoms become 'invisible' in XAFS fitting.[82,83] The U-N 2nd shell did not show missing atoms (8.0 in fitting vs. 8.0 in theory), change of distance (4.21 Å in fitting vs 4.22 Å in theory), nor shell separation. The Debye-Waller factor of U-N 2nd path is larger than other paths (19.2×10^{-3} Å^{-2}).

Overall, the XAFS fitting result suggests degrees of distortions in various CN shells. Such alteration in the rock salt structure may be due to slight oxygen diffusion into the lattice or additional N diffusing through the structure yielding the secondary $UN_{1.5+x}$ phase (not accounted for in the EXAFS fitting), which is also implied by the synchrotron XRD result (Figure 1). It should be noted that the surface oxidation of UN (and the subsequent formation of $UN_{1.5+x}$) may have occurred during the sample shipment to XAFS or XRD measurements, due to the susceptibility of UN to oxidation despite the preventative measures employed during sample loading and transport.

3.2 Step-wise thermal oxidation of UN in air

The general progression of the stepwise thermal oxidation of UN in synthetic air is depicted in Figure 3, from which TGA-DSC analysis was used as the primary method for the investigation of oxidative processes and the determination of the corresponding stoichiometric mass changes. To elucidate the molar ratios of products and intermediates formed during the stepwise oxidation of

UN, MS analyses of the evolved or consumed gas were performed and exhibited in conjunction with the TGA result (Figure 3). From the TGA results (Table 1), the starting phase composition of the UN sample was calculated to have a chemical formula of $UN \cdot 0.007UN_{1.5+x} \cdot 0.0035UO_2$ (normalized to one mole of UN and using $UN_{1.5+x}$ to represent U_2N_{3+x}[46,52]) in good agreement with the speculated formula from XRD analysis. Such proposed chemical composition is consistent with the passivating "sandwich" layer [46,47] formed on UN due to potential exposure to oxygen prior to the TGA-MS-DSC analysis. The TGA-derived molar ratio of the layer in relation to the total bulk UN sample is in qualitative agreement with previous thermal oxidation studies.[46] To evaluate the growth of the passivating layer under ambient handling or storing conditions, we performed a long dwelling (12 hours) isothermal TGA study at 27 °C in synthetic air (Figure S6a). The ambient isothermal TGA revealed a rapid mass gain (+0.16 wt. %) in the first 60 minutes, followed by a much slower mass gain (a total of +0.24 wt. %) after 12 hours, with the rate of mass gain fitted by an exponential decay function (Figure S7b). This result agrees with our XRD analysis of UN exposed to ambient environment (Figure 6) and previous surface oxidation experimental [47] and theoretical [81] studies of UN, which can be qualitatively described by the following process [46,47,81,84,85]:

$$UN_z + (y/2)\ O_2 \rightarrow UN_{z-x}O_y^{\ddagger} \quad (1)$$

$$UN_{z-x}O_y^{\ddagger} \rightarrow (1/2)\ UO_{1+y} + (1/2)\ UN_{z+x} + (x/4)\ N^{*} \quad (2)$$

$$(1/2)\ UN_z + (x/4)\ N^{*} \rightarrow (1/2)\ UN_{z+x} \quad (3)$$

where $UN_{z-x}O_y^{\ddagger}$ corresponds to UN surface saturation by oxygen and the formation of a surface uranium oxynitride,[47,81] N^{*} refers to the displaced nitrogen by oxygen absorption and disproportionation of $UN_{z-x}O_y^{\ddagger}$,[46] z and y are ~1, and x is ~0.5 (for reactions 1-3).[81] The corresponding molar ratio of $UN \cdot 0.007UN_{1.5+x} \cdot 0.0035UO_2$ after 12 hours of isothermal ambient treatment is approximately $UN \cdot 0.008UN_{1.5+x} \cdot 0.004UO_2$ (normalized to one mole of UN). However, it should be noted that any UO_2 formed on UN during ambient oxidation is likely poorly crystalline according to Figure 6. This is in agreement with previous surface oxidative studies that surface oxidation of UN at ambient temperature is a kinetically hindered process, and the formed passivating layer greatly reduces the extent of bulk oxidation.[46,47,81,84] According to current and previous calorimetric investigations, [52] all these phases are thermodynamically stable at

room temperature with α-$UN_{1.5+x}$ being the most stable. This may explain the preferentiality of UN to form an UO_2 - $UN_{1.5+x}$ passivating layer during thermal oxidation processes.[46] During the initial stages of oxidation the surface UN layer reacts readily with oxygen forming the $UN_{z-x}O_y^{\ddagger}$ surface intermediate (reaction 1) and liberating N*, which at lower temperatures (< 100° C) does not readily form molecular N_2 but rather dissolves into the UN lattice (or the $UN_{z-x}O_y^{\ddagger}$ - UN layer interphase), providing sufficient nitrogen for the conversion of rock salt UN to BCC α-$UN_{1.5+x}$.[46,47] The presence of $UN_{z-x}O_y$ on the surface of α-$UN_{1.5+x}$ inhibits further absorption of O_2, greatly hindering further oxidative progression at room temperature (Figure 6 and Figure S7a).[47]

A previous surface oxidation study of non-stoichiometric uranium nitrides demonstrated that the $UN_{z-x}O_y$ phase is primarily found on $UN_{1.66}$ oxidized films.[47] At higher temperatures (or prolonged exposure) $UN_{z-x}O_y$ has been shown to disproportionate into the epitaxially oriented $UO_2 \cdot UN_{1.5+x}$ passivating layer described by Dell.[46] The formation of the passivating layer and its protective properties can further be understood from the crystallographic viewpoint. UN possesses a rock salt structure (space group $Fm\bar{3}m$) where U atoms are in the face-center cubic (FCC) sublattice (U-U pair distance at 3.46 Å).[86] In the converted phases, α-$UN_{1.5+x}$ (space group $Ia\bar{3}$) and UO_2 (space group $Fm\bar{3}m$) also have FCC arrays of U atoms, although with slightly increased distance of the U-U pairs with interatomic distances of 3.76 Å and 3.87 Å, respectively.[46,87] Thus, the conversion from UN to its alteration phases will have small shear resistance from the metal sublattices with only oxygen diffusing into the anion sublattices for reconstruction. Such crystallographic continuation may promote cohesive growth of the passivating $UO_2 \cdot UN_{1.5+x}$ layer that allows retention of macroscopic integrity and minimal cracking that may slow down further oxidation.[46,88] It is worth noting that the reason of discussing UN surface oxidation here was for interpreting our thermogravimetric analysis results, while previous studies focused on quantitative kinetic analyses.[46,47,81,84,85]

The bulk oxidation of $UN \cdot 0.007UN_{1.5+x} \cdot 0.0035UO_2$ has an onset temperature of 389 °C (Figure 3), accompanied by a rapid mass gain and a strong exothermic heat effect. Such onset temperature is higher than previously reported (250 °C [39] and 290 °C [47] in oxygen). The enhanced resistance to thermal oxidation may be due to the gradual growth and thickening of the previously mentioned $UN_{1.5+x} \cdot UO_2$ passivating layer formed in air during progressive temperature increase in the TGA-DSC experiment, where +2.37 wt. % was recorded between 30 °C to 389 °C

(Table 1 and Figure 3). The gradual growth of the passivating layer was also suggested by the lack of accompanying heat signals. Thus, at 389 °C prior to rapid bulk oxidation, the chemical composition of the sample was approximated to be $UN{\cdot}0.022UN_{1.5+x}{\cdot}0.011UO_2$. Moreover, the growth rate of the passivating layer has an acceleration at around 230 °C, in agreement with a previous oxidative study of UN by Dell *et al.*,[46] where the formation of UO_2 and α-$UN_{1.5+x}$ on the UN surface were revealed by XRD but only after heat treatments at temperatures of ≥280 °C, our results on ambient oxidation of UN (Figure 6) demonstrated that crystalline α-$UN_{1.5+x}$ and β-$UN_{1.5-x}$ forms on UN even at ambient temperatures, while any oxides formed likely require higher temperatures (≥280 °C) to achieve sufficient crystallinity.

In situ MS analysis reveals that the bulk oxidation of $UN{\cdot}0.007UN_{1.5+x}{\cdot}0.0035UO_2$ between 360 °C and 460 °C was accompanied by rapid release of various gases with the amount N_2 >> NO_2 > NO, corresponding to *m/z* =28, *m/z* = 44, *m/z* = 30, respectively, and the concurrent consumption of O_2 (*m/z* = 16 signal) (Figures 3 and S5). Because the N_2 signal is several orders of magnitude higher than those of the NO_2 and NO signals (Figure S6), N_2 was used as the primary nitrogen species for sequential MS analyses (Table 2). To further evaluate the mechanism of the thermal oxidation of $UN{\cdot}0.007UN_{1.5+x}{\cdot}0.0035UO_2$ and the chemical stoichiometries of its intermediate products, we preformed Gaussian deconvolution on the TGA, MS (N_2 and O_2), and heat flow profiles (Figure 4), where three temperatures of interest were specifically marked for 389 °C, 414 °C, and 464 °C, corresponding to the onset temperatures for the subsequent $UN{\cdot}0.022UN_{1.5+x}{\cdot}0.011UO_2$ oxidative processes (steps 3 and 4 in Table 1 from TGA results, and 1 and 2 in Table 2 from MS results). From 389 °C to 414 °C, $UN{\cdot}0.022UN_{1.5+x}{\cdot}0.011UO_2$ underwent a rapid mass increase of +9.98 wt. % (step 3 in Table 1). The Gaussian deconvolution analyses of the first derivate of mass gain with respect to temperature, the DSC heat flow, and the MS *m/z* =28 signal suggest two simultaneously occurring oxidation processes. The first reaction can be described by the following:

$$(1-1.5y)UN{\cdot}(y)UN_{1.5+x}{\cdot}(y/2)UO_2 + (3-z-y)\,O_2 \rightarrow (z)UO_2{\cdot}(1-z)UO_3{\cdot}N_k + (1-k)/2\,N_2 \quad (4)$$

in which *x, y, z, k* denote molar non-stoichiometric coefficients unique to the nature of the starting UN sample (surface area, impurities, preparation methods),[39,46,89] the amounts of oxygen and nitrogen present in the oxidative environment,[90] and the thermal condition governing the

oxidative process (e.g., heating rate and temperature profile).[46,48] Additionally, the description of the oxidative process using non-stoichiometric coefficients may be useful in the estimation of dependent chemical disproportionation. Thus, experimentally quantifying one of the specie's coefficients may yield insights to the concentrations of other components during the oxidative process. The formation of possibly concurrent UO_2 and UO_3 was suggested by previous oxidation studies on UN and uranium oxides,[39,46,91] and their thermal stabilities. From the quantitative analyses provided in this work, we estimated $y \approx 0.022$, $z \approx 0.30$, $k \approx 0.33$ using TGA to calculate the approximate y and z values and MS signal integration and partition to estimate the k value (Tables 1 and 2). The obtained y, z, and k parameters are in general agreement with TGA, DSC, and MS results. The x coefficient was set to 0 for simplicity, which would not significantly influence the results as long as it fell in the range of $0 < x < 0.2$.[52] The second oxidation process occurred between 414 °C and 464 °C corresponding to a release of N_2 and a consumption of O_2 along with a gradual increase in mass (+1.10 wt. %) (Figure 4, Tables 1 and 2), as a result of further oxidation of UO_2 to UO_3 [39,46]:

$$(z)UO_2 \cdot (1 - z)UO_3 \cdot N_k + (z/2)\ O_2 \rightarrow UO_3N_{k-l} + (l/2)\ N_2 \quad (5)$$

The coefficient l, the nitrogen released, was derived to be around 0.15 from our MS analysis, yielding $UO_3N_{0.18}$ at 464 °C, which corresponds to a total mass gain of +13.45 wt. %. This result is in excellent agreement with a previous study by Dell *et al.* which yielded $UO_3N_{0.2}$ to $UO_3N_{0.4}$ as the final product from the isothermal oxidation of UN.[46] Here the nitrogen, hypothesized to be dissolved in the UO_3 structure, has excellent thermal stability.[46] This was confirmed by our MS analysis indicating that the remaining nitrogen was fully evolved at 562 °C (Figures S4 and 3) corresponding to a mass loss of -0.31 wt. % due to the following reaction:

$$UO_3N_{k-l} \rightarrow UO_3 + (k - l)/2\ N_2 \quad (6)$$

Above 562 °C, a continuous mass loss was observed with a concurrent broad MS O_2 release signal (Figure S5) and a broad heat flow (Figure 3), suggesting the decomposition of UO_3 to U_3O_8[72,92]:

$$UO_3 \rightarrow (1/3)\ U_3O_8 + (1/6)\ O_2 \quad (7)$$

However, according to the TGA result (Table 1, Figure 5), the measured mass loss at 900 °C (-0.93 wt. %) is significantly lower than the expected mass loss (-1.95 wt. %), meaning that the decomposition was not fully complete at 900 °C, consistent with its sluggish reaction nature.

We further compared the oxidative processes of $UN{\cdot}0.007UN_{1.5+x}{\cdot}0.0035UO_2$ with that of UO_2[93] in Figure 5. Both data were collected on the same instrument (SetSYS 2400) and the mass change signal was normalized to reflect molar mass of analyzed samples using $UN{\cdot}0.007UN_{1.5+x}{\cdot}0.0035UO_2$ molar ratio (254.54 g/mol) as the initial molar mass of UN and 270.03 g/mol as for UO_2. The onset temperatures of bulk oxidations are 349° C and 389° C for UO_2 and $UN{\cdot}0.007UN_{1.5+x}{\cdot}0.0035UO_2$, respectively (Figure 5), suggesting that UN possesses greater resistance to bulk oxidation than UO_2 under a flowing air atmosphere. Further difference between the oxidation processes of UN and UO_2 can be noted by the molar masses of the final products formed during the oxidation reactions. At 900 °C, the oxidation product of UO_2 possesses a molar mass of 280.25 g/mol, close to that of U_3O_8 (280.70 g/mol normalized to one mole of U), while the final product from the $UN{\cdot}0.007UN_{1.5+x}{\cdot}0.0035UO_2$ oxidation possesses has a molar mass of 285.62 g/mol corresponding to $0.88UO_3{\cdot}0.12U_3O_8$, i.e., a mixture of UO_3 and U_3O_8. Nevertheless, it should be noted that at 900 °C in air, the mass change of UO_2 is approximately constant, indicating continuous oxidation of $U(IV)O_2$ to U_3O_8. On the other hand, the reduction of pentavalent U oxide phase (from the bulk oxidation of $UN{\cdot}0.007UN_{1.5+x}{\cdot}0.0035UO_2$) did not lead to a full conversion to U_3O_8, suggesting a gradually process which could also be kinetically hindered.[91] Additionally, our *ex situ* synchrotron XRD results conducted on UN oxidized to 900 °C (Figure 6) using similar conditions to that of our TGA experiments indicated that the final product of UN oxidation is a poorly crystalline mixture of α -U_3O_8 and β-U_3O_8 [94]. This indicates that if UO_3 is present at 900 °C it is highly amorphous and is likely a resultant of the kinetically hindered nature of the reaction. Future *in situ* high temperature XRD studies of UN oxidation are required to derive the phase relationships and thermal oxidation mechanisms indicated by TGA-MS analyses.

3.3 High Temperature Drop Calorimetry

Two types of high temperature drop calorimetric measurements were performed on UN samples. Since loading the UN samples for TGA-MS-DSC analysis required similar duration of time (exposure of the samples to air) as dropping the samples into the calorimetric chambers, the

$UN{\cdot}0.007UN_{1.5+x}{\cdot}0.0035UO_2$ molar ratio formula (determined from TGA) was used as the starting composition of the UN samples.

The first type of experiment preformed was high temperature transposed temperature drop calorimetry (under continuously flowing oxygen), with its results shown in Table 3. XRD and XAFS was conducted on the oxidized UN samples (Figure S8 and Figure 2 respectively) recovered from the transposed temperature drop calorimetry to check the phase as in the final product used in the thermochemical cycles (Table 3). α-U_3O_8 was identified as the dominant phase with minor presence of β-U_3O_8, in agreement with our TGA-DSC analysis (however conducted under air) and consistent with previous transposed drop calorimetric studies on USi, U_3Si_2, and U_3Si_5.[49,50] The benchtop XRD results (Figure S8) are likewise consistent with that obtained from the synchrotron on UN oxidized to 900 °C in air (Figure 6). To further examine the U_3O_8 phase formed during UN oxidation experiments, we collected XAFS spectrum of the sample oxidized to 900 °C (Figures 2d and 2e), which is similar to the spectrum of previously reported α-U_3O_8.[61,95] Using the α-U_3O_8 structural model (Figure 2e) generates sufficient XAFS fit (Table S2), matching all 5 theoretical U-O paths with distance differences between all theoretical and experimental U-O paths being only 0.05 Å. To further understand the structural characteristics of oxidized UN sample, it is important to investigate all U-U paths. However, similarly to XAFS of U, missing U-U CNs were likewise identified, suggesting the phase formed during UN oxidation possesses α-U_3O_8 long-range ordered structure with distortions in the local coordination environment of U atoms.

The formation of U_3O_8 as the final oxidation product was further confirmed by heating the recovered samples isothermally at 750 °C for 5 hours in air and yielded only a slight drift of the mass variance (Figure S9), with no changes in the heat flow signal, suggesting no further reaction or transformation. Lastly, the quartz crucible used for transposed calorimetric experiments (Figure S10a) showed black pulverized spots on the inner quartz lining, again confirming the presence of U_3O_8.[96] With $UN{\cdot}0.007UN_{1.5+x}{\cdot}0.0035UO_2$ and U_3O_8 as the starting and final phases respectively in the transposed drop calorimetric experiments, we directly measured the enthalpic change corresponding to the thermal oxidation of $UN{\cdot}0.007UN_{1.5+x}{\cdot}0.0035UO_2$ at 700 °C (reaction 1 in Table 3), which was also denoted as enthalpy of transposed drop, $\Delta H_{td} = -865.4 \pm 13.8$ kJ/mol. Such enthalpic value was used in the thermochemical cycle (Table 3) to derive the enthalpy of oxidation of UN to U_3O_8 ($\Delta H_{ox,U3O8}$) at ambient condition to be $\Delta H_{ox,U3O8} = -455.3 \pm 6.9$ kJ/mol·atom. This value is in excellent agreement with the enthalpy of ignition of UN to U_3O_8 (at

room temperature) which was estimated by Dell *et al.* to be – 447.7 kJ/mol·atom (sign inverted from the original work to correspond with the standard notation and normalized per mole atom of UN).[46] Lastly, the newly determined $\Delta H_{ox,U3O8}$ was used to calculate the standard enthalpy of formation of UN from its elements ($\Delta H°_f$) to be – 138.8 ± 6.9 kJ/mol·atom (Table 3). This value is slightly more endothermic compared with the accepted standard enthalpy of formation of UN: –145.0 ± 1.5 kJ/mol·atom (selected value from the thermochemical review of uranium compounds [52]). This may be due to the incomplete oxidation of UN to U_3O_8 in an oxygen environment at 700° C, with the final product likely containing small amounts (< 4 wt. %) of incompletely oxidized U_3O_7, U_4O_{9+x} and other related phases [49,50,52,93] undetectable by lab-based XRD due to their relatively low abundances. To address any concern of the incomplete oxidation of uranium oxides in the final product, we performed a second type high temperature drop calorimetric experiment using sodium molybdate oxide melt as solvent (high temperature oxide melt drop solution calorimetry). The dissolution of intermetallic uranium compound in the molten $3NaO{\cdot}4MoO_3$ solvent led to its oxidation to the hexavalent state, [49,50] a definitive final state to be used in the thermochemical cycle. Figure S10b shows the quartz crucible containing the molten solvent and the oxidized $UN{\cdot}0.007UN_{1.5+x}{\cdot}0.0035UO_2$ product dissolved within upon immediate removal from the calorimeter's reaction chamber (700 °C). The molten salt has a transparent orange color indicative of the full dissolution of UN. Thus, dissolved hexavalent uranium was chosen as the final state of $UN{\cdot}0.007UN_{1.5+x}{\cdot}0.0035UO_2$ after calorimetry. The enthalpy of drop solution (ΔH_{ds}) was measured directly as ΔH_{ds} = – 944.4 ± 11.5 kJ/mol (for reaction 1 in Table 4), which was then used in the thermochemical cycle in Table 4 to derive the enthalpy of oxidation of UN to UO_3 at ambient conditions, $\Delta H_{ox,UO3}$ = – 465.8 ± 5.8 kJ/mol·atom. Using the newly obtained $\Delta H_{ox,UO3}$ and $\Delta H_{ox,U3O8}$ values, we calculated the enthalpy of oxidation of U_3O_8 to UO_3 at room temperature, expressed by the reaction:

$$1/3\ U_3O_{8\ (s,\ 25°\ C)} + 1/6\ O_{2\ (g,\ 25°\ C)} \rightarrow\ UO_{3\ (s,\ 25°\ C)} \qquad (8)$$

yielding $\Delta H_{ox,U3O8\rightarrow UO3}$ = –21.0 ± 12.5 kJ/mol. This value is less exothermic compared with the published value $\Delta H_{oxU3O8\rightarrow UO3}$ = –32.3 ± 2.6 kJ/mol, determined from previous calorimetric measurements of metastudtite ($(UO_2)O_2(H_2O)_2$) [65]. The origin of high error on the newly calculated $\Delta H_{ox,U3O8\rightarrow UO3}$ value stems from propagation of uncertainty from the highly exothermic signals (ΔH_{td}, ΔH_{ds}) of UN oxidation. Additionally, the newly calculated value is slightly endothermic compared to that extracted from previous calorimetric measurements [65]. As

discussed above, this may likewise be due to the incomplete oxidation of uranium oxides by transposed temperature drop calorimetry at 700 °C.

The standard enthalpy of formation from the elements was calculated for UN using the value of $\Delta H_{ox,UO3}$, yielding $\Delta H°_f$ = – 144.4 ± 5.9 kJ/mol·atom, which is consistent with that from the first type calorimetry and particularly in excellent agreement with previously reported $\Delta H°_f$ of UN (normalized per mole atom of UN from the original work) to be – 145.2 ± 1.1 kJ/mol·atom obtained by fluorine bomb calorimetry [51] or – 147.7 ± 2.1 kJ/mol·atom by transposed drop calorimetry with Pt sample encapsulation [97]. Thus, $\Delta H°_f$ = – 144.4 ± 5.9 kJ/mol·atom is chosen as the new benchmark enthalpy value for UN. A correction to the $\Delta H_{ox,U3O8\rightarrow UO3}$ value can now be made assuming that the enthalpy contribution from the incomplete oxidation of minor oxides with the U_3O_8 (formed during transposed drop calorimetric measurements) is proportional to the difference between the $\Delta H°_f$ values obtained from transposed drop (incomplete oxidation) and drop solution (complete dissolution and oxidation), $\Delta H°_{f,UO3}$ - $\Delta H°_{f,U3O8}$ = – 11.2 kJ/mol. Applying this enthalpic correction to the $\Delta H_{ox,U3O8\rightarrow UO3}$ yielded the corrected value of – 32.2 ± 18.0 kJ/mol, in excellent agreement with value extracted from previous calorimetric measurements by Guo *et al*. [65]. The agreement between the two independently determined $\Delta H_{ox,U3O8\rightarrow UO3}$ values further validates the concurrent use of transposed temperature drop calorimetry and drop solution calorimetry for the determination of enthalpies of interest.

The advantages of using high temperature transposed drop and drop solution calorimetry for the study of uranium intermetallic compounds are as followed. First, both of these techniques can be used independently to measure the enthalpies of oxidation/transformations of uranium compounds to different final oxidative states.[49,50,65] Transposed temperature calorimetry performed in an oxidative environment prefers the formation of U_3O_8 or similar phases with non-stoichiometric oxygen defects depending on the oxygen partial pressure in the calorimeter reaction chamber).[49,50] On the other hand, drop solution calorimetry favors the complete dissolution of the uranium oxides and the conversion of lower-valence U to the hexavalent state.[49,69–71,73] Thus, drop solution calorimetry may be used as an effective method to calculate enthalpies of formation of uranium compounds when the formation of stoichiometric U_3O_8 is ambiguous. Furthermore, the ability to directly measure the enthalpies of U oxidation to different final states allows extrapolation of other intermediate reactions, which is typically difficult to obtain directly. Lastly, both high temperature drop calorimetry are highly adaptable and can be applied to a wide

variety of uranium compounds with relative ease, allowing rapid and accurate accumulation of thermal data, which can help fill thermochemical data gaps and confirm/update enthalpic values obtained by other methods.

The effects of nitrogen non-stoichiometry on the standard enthalpy of formation of UN (and related $UN_{1.5\pm x}$ phases) were exhibited in Figure 7 by combining the present and previously published $\Delta H°_f$ values[52]. A negative linear correlation exists between $\Delta H°_f$ and the N/U molar ratio. The origin of this trend is likely due to structural changes experienced by U-N phases upon incorporation of nitrogen, as discussed above (section 3.2), primarily being driven by the thermodynamic stability of the body-center cubic (BCC) α-$UN_{1.5+x}$ phase in relation to the rock salt-type phase of UN and the La_2O_3-type β-$UN_{1.5-x}$.[46,98,99] This suggests that a slight hyper-stoichiometry of nitrogen may be stabilized in the UN matrix due to thermodynamically favorable effects of N* incorporation into the UN aristotype structure thus explaining the presence of α-$UN_{1.5+x}$ within the pristine UN sample, and its continuous formation on UN surface upon prolonged exposure to ambient environment.

Lastly, we compared the thermodynamic stabilities of several intermetallic nuclear fuel candidates, including UC, USi, U_3Si_5, and U_3Si_2 (Table 5). The enthalpic values of uranium silicides were recently determined by high temperature drop calorimetric measurements.[49,50] The values for UC were previously obtained from bomb calorimetry.[46,100] The enthalpies of oxidation at standard condition are normalized per mole atom and follow the trend: U_3Si_2 < USi < U_3Si_5 < UC < UN, while the standard enthalpies of formations follow an inverse trend: UN < UC < U_3Si_5 < USi < U_3Si_2. This demonstrates that UN is least susceptible to oxidation and has the highest thermodynamic stability among the intermetallic fuel candidates. This does not imply that uranium silicides or carbides should be excluded from consideration for the next generation nuclear reactors, since each compound possesses unique advantages in fuel fabrication, neutronic, thermophysical properties and chemical compatibilities. Rather, mixed intermetallic phases or enhanced intermetallic fuels doped with various elements may likely be the solution, which, however require further studies in the future.[101–104]

4. Conclusions

In this work, bulk thermal oxidation of UN was examined using *in situ* TGA-MS-DSC, and high temperature transposed drop and oxide melt drop solution calorimetry. Our results indicate

that UN can be effectively protected from extended oxidation presumably due to the formation of a thin passivating layer, suggested by a prolonged ambient oxidation TGA. The passivating layer was hypothesized to greatly hinder the onset of the bulk oxidation up to 389 °C. From 389 °C to 414 °C, UN undergoes a highly exothermic reaction resulting in a significant mass gain. This process was determined by TGA-MS to correspond to the bulk oxidation of UN to $0.30UO_2 \cdot 0.70UO_3 \cdot 0.33N$ followed by a gradual conversion to UO_3 (completed at 562 °C) and release of nitrogen. UO_3 was then sluggishly decomposed to U_3O_8. A full conversion of UO_3 to U_3O_8 was not complete at least up to 900 °C. The energetics of formation of UN was investigated by high temperature transposed drop and oxide melt drop solution calorimetric measurements. UN was demonstrated to be thermodynamically favorable to be oxidized to both UO_3 and U_3O_8 at ambient conditions. The standard enthalpies of formation for UN were determined by both types of calorimetric methods, yielding – 138.8 ± 6.9 kJ/mol·atom (from transposed drop experiments) and – 144.4 ± 5.9 kJ/mol·atom (from oxide melt drop solution experiments), the latter of which we consider as the new experimental benchmark value. Both values are consistent with previously determined standard enthalpies of formation of UN based on high temperature oxidative dissolution experiments. Combining the enthalpy value of UN from this work with those previously determined for β-$UN_{1.5-x,}$ and α-$UN_{1.5+x}$, the energetic landscape of the U-N system emerges, revealing a negative linear correlation between the standard enthalpies of formations and the N/U molar ratio. Lastly, the thermodynamic stability of UN was demonstrated to be better than other intermetallic nuclear fuels of interest.

Acknowledgements

This work was supported by the institutional funds from the Department of Chemistry and New Faculty Seed Grant from ORAP at Washington State University, and by the U.S. Department of Energy, Office of Nuclear Energy, grant DE-NE0008582. Research presented in this article was also supported by the Laboratory Directed Research and Development (LDRD) program via projects 20180007DR and 20220053DR at Los Alamos National Laboratory (LANL). VGG acknowledges the support of the Seaborg Institute through a LANL Seaborg graduate fellowship. LANL, an affirmative action/equal opportunity employer, is managed by Triad National Security Administration of the U.S. Department of Energy under contract number 89233218CNA000001. Portions of this research were supported by collaboration, services, and infrastructure through the

Nuclear Science Center User Facility at WSU, the WSU-PNNL Nuclear Science and Technology Institute, and Alexandra Navrotsky Institute for Experimental Thermodynamics. This research used resources of the Advanced Photon Source, a U.S. Department of Energy (DOE) Office of Science User Facility operated for the DOE Office of Science by Argonne National Laboratory under Contract No. DE-AC02-06CH11357.

Tables:

Table 1 TGA mass changes (%) of UN under a flowing air atmosphere compared with theoretical values expected for the simplified oxidative reactions

Oxidation steps	Temperature (°C)	Experimental Mass Change (%)	Theoretical Mass Change (%)	Difference (%)*
(1) $UN \rightarrow UN{\cdot}0.007UN_{1.5+x}{\cdot}0.0035UO_2$	30	+1.00	+1.09	0.09
(2) $UN{\cdot}0.007UN_{1.5+x}{\cdot}0.0035UO_2 \rightarrow UN{\cdot}0.022UN_{1.5+x}{\cdot}0.011UO_2$	30 – 394	+2.37	+2.32	0.05
(3) $UN{\cdot}0.022UN_{1.5+x}{\cdot}0.011UO_2 \rightarrow 0.30UO_2{\cdot}0.70UO_3{\cdot}0.33N$	389 – 414	+9.98	+9.72	0.26
(4) $0.30UO_2{\cdot}0.70UO_3{\cdot}0.33N \rightarrow UO_3{\cdot}0.18N$	414 – 464	+1.10	+0.97	0.13
(5) $UO_3{\cdot}0.18N \rightarrow UO_3$	464 – 562	-0.31	– 0.87	0.56
(6) $UO_3 \rightarrow U_3O_8$	≥562	-0.93	– 1.95	1.02

* Difference = |experimental mass change - theoretical mass changes|

Table 2. Evolved gas MS analysis for the corresponding UN oxidation steps.

Oxidation Steps	Temperature (°C)	Nitrogen Fraction (mol %)*			Oxygen Fraction (mol %)*		
		Exp.	Theo.	Diff. %†	Exp.	Theo.	Diff. %†
(1) $UN{\cdot}0.022UN_{1.5+x}{\cdot}0.011UO_2 \rightarrow 0.30UO_2{\cdot}0.70UO_3{\cdot}0.33N$	394 – 414	–66.37	–67.00	0.63	+83.43	+89.27	5.84
(2) $0.30UO_2{\cdot}0.70UO_3{\cdot}0.33N \rightarrow UO_3{\cdot}0.18N$	414 – 464	–15.12	–15.00	0.12	+16.57	+10.73	5.84
(3) $UO_3{\cdot}0.18N \rightarrow UO_3$	464 – 562	–18.51	–18.00	0.51	–	–	–
(4) $UO_3 \rightarrow U_3O_8$	≥562	–	–	–	–14.54	–11.11	3.43

* Mol % of evolved gasses were determined from the ratio of integrated gas signals through the temperature range of the corresponding reactions, and the summation of the total integrated gas signal for each gas; † Diff. represents the absolute % difference between the theoretical and experimentally determined integrations of gas signals.

Table 3. Thermochemical cycles used for calculations of the standard enthalpy of formation of UN ($\Delta H°_f$) based on the transposed temperature drop calorimetric data of UN under flowing oxygen at 700 ºC.

Reaction	**ΔH (kJ/mol)**
(1) $UN_{(s,\ 25\ °C)} + 0.0035UO_{2(s,\ 25\ °C)} + 0.007\ UN_{1.5(s,\ 25\ °C)} + 1.330\ O_{2(g,\ 700\ °C)} \rightarrow \frac{1}{3}\ U_3O_{8(s,\ 700\ °C)} + \frac{1}{2}\ N_{2(g,\ 700\ °C)}$	$\Delta H_1 = \Delta H_{td} = -865.41^a \pm 13.80^b\ (4)^c$
(2) $O_{2(g,\ 25\ °C)} \rightarrow O_{2(g,\ 700\ °C)}$	$\Delta H_2 = 21.8$[105]
(3) $N_{2(g,\ 25\ °C)} \rightarrow N_{2(g,\ 700\ °C)}$	$\Delta H_3 = 20.7$[106]
(4) $U_3O_{8(s,\ 25\ °C)} \rightarrow U_3O_{8(s,\ 700\ °C)}$	$\Delta H_4 = 191.5$[50]
(5) $U_{(s,\ 25\ °C)} + \frac{3}{4}\ N_{2(g,\ 25\ °C)} \rightarrow UN_{1.5(s,\ 25\ °C)}$	$\Delta H_5 = -366.5 \pm 5.0^*$[52]
(6) $U_{(s,\ 25\ °C)} + O_{2(g,\ 25\ °C)} \rightarrow UO_{2(s,\ 25\ °C)}$	$\Delta H_6 = -1085.0 \pm 1.0$[107]
(7) $U_{(s,\ 25\ °C)} + \frac{4}{3}\ O_{2(g,\ 25\ °C)} \rightarrow \frac{1}{3}\ U_3O_{8(s,\ 25\ °C)}$	$\Delta H_7 = -1191.6 \pm 0.8$[50]

Enthalpy of oxidation of UN per mol atom to U_3O_8 and N_2:

$UN_{(s,\ 25\ °C)} + 0.00\ 35UO_{2(s,\ 25\ °C)} + 0.007\ UN_{1.5(s,\ 25\ °C)} + 1.33\ O_{2(g,\ 25\ °C)} \rightarrow \frac{1}{3}\ U_3O_{8(s,\ 25\ °C)} + \frac{1}{2}\ N_{2(g,\ 25\ °C)}$

$$\Delta H_{ox,U3O8}(UN) = (\Delta H_{td} + 1.33\ \Delta H_2 - \tfrac{1}{2}\ \Delta H_3 - \tfrac{1}{3}\ \Delta H_4) / 2$$
$$= -455.3 \pm 6.9\ \text{kJ/mol·atom}$$

Standard enthalpy of formation of UN per mole atom:

$0.9895\ U_{(s,\ 25\ °C)} + 0.4948\ N_{2(g,\ 25\ °C)} \rightarrow 0.9895\ UN_{(s,\ 25\ °C)}$

$$\Delta H°_f(UN) = ((-2\Delta H_{ox}(UN) - 0.007\ \Delta H_5 - 0.0035\ \Delta H_6 + \Delta H_7)/0.9895)/2$$
$$= -138.8 \pm 6.9\ \text{kJ/mol·atom}$$

[a]Averaged value; [b]Two standard deviations of the average value; [c]Number of measurements
[*]value for $UN_{1.5}$ extrapolated from ref [52].

Table 4. Thermochemical cycles used for calculations of the standard enthalpy of formation of UN ($\Delta H°_f$) based on drop-solution calorimetric data of UN in molten sodium molybdate at 700 ºC.

Reaction	**ΔH (kJ/mol)**
(1) $UN_{(s,\ 25\ °C)} + 0.0035\ UO_{2(s,\ 25\ °C)} + 0.007\ UN_{1.5(s,\ 25\ °C)} + 1.497\ O_{2(g,\ 700\ °C)} \rightarrow UO_{3(sln,\ 700\ °C)} + ½\ N_{2(g,\ 700\ °C)}$	$\Delta H_1 = \Delta H_{ds} = –944.40^a \pm 11.49^b\ (4)^c$
(2) $O_{2(g,\ 25\ °C)} \rightarrow O_{2(g,\ 700\ °C)}$	$\Delta H_2 = 21.8$[105]
(3) $N_{2(g,\ 25\ °C)} \rightarrow N_{2(g,\ 700\ °C)}$	$\Delta H_3 = 20.7$[106]
(4) $\gamma\text{-}UO_{3(s,\ 25\ °C)} \rightarrow UO_{3(sln,\ 700\ °C)}$	$\Delta H_4 = 9.5 \pm 1.5$ [73,91]
(5) $U_{(s,\ 25\ °C)} + ¾\ N_{2(g,\ 25\ °C)} \rightarrow UN_{1.5(s,\ 25\ °C)}$	$\Delta H_5 = –366.5 \pm 5.0^*$[52]
(6) $U_{(s,\ 25\ °C)} + O_{2(g,\ 25\ °C)} \rightarrow UO_{2(s,\ 25\ °C)}$	$\Delta H_6 = –1085.0 \pm 1.0$[107]
(7) $U_{(s,\ 25\ °C)} + {}^3/_2\ O_{2(g,\ 25\ °C)} \rightarrow UO_{3(s,\ 25\ °C)}$	$\Delta H_7 = –1223.8 \pm 0.8$[108]

Enthalpy of oxidation of UN per mol atom to UO_3 and N_2:

$UN_{(s,\ 25\ °C)} + 0.0035\ UO_{2(s,\ 25\ °C)} + 0.007\ UN_{1.5(s,\ 25\ °C)} + 1.497\ O_{2(g,\ 25\ °C)} \rightarrow UO_{3(s,\ 25\ °C)} + ½\ N_{2(g,\ 25\ °C)}$

$\Delta H_{ox,UO3}(UN) = (\Delta H_{ds} + 1.497\ \Delta H_2 – ½\ \Delta H_3 – \Delta H_4) / 2$
$= – 465.8 \pm 5.8$ kJ/mol·atom

Standard enthalpy of formation of UN per mole atom:

$0.9895\ U_{(s,\ 25\ °C)} + 0.4948\ N_{2(g,\ 25\ °C)} \rightarrow 0.9895\ UN_{(s,\ 25\ °C)}$

$\Delta H°_f(UN) = (– 2\Delta H_{ox}(UN) – 0.007\ \Delta H_5 – 0.0035\ \Delta H_6 + \Delta H_7)/0.9895)/2$
$= –144.4 \pm 5.9$ kJ/mol·atom

[a]Averaged value; [b]Two standard deviations of the average value; [c]Number of measurements
[*] value for $UN_{1.5}$ extrapolated from ref [52].

Table 5. Enthalpic values of interest for the selected intermetallic fuel compounds.

Compound	Final oxide‡	ΔH_d (kJ/mol)	ΔH_{ox} (kJ/mol·atom)	$\Delta H°_f$ (kJ/mol·atom)
UN	U_3O_8 (s, 700° C)	–865.41 ± 13.80	–455.3 ± 6.9	–144.4 ± 5.9
	UO_3 (sln, 700° C)	–944.40 ± 11.49	–465.8 ± 5.8	
UC [46,100]	U_3O_8 (unspecified)	–	–748.9[46]	–48.5 ± 2.0§[100]
	–	–	–	
U_3Si_5 [50]	U_3O_8 (s, 700° C)	–6508.02 ± 58.03†	–836.42 ± 7.25†	–43.8 ± 9.0*
	–	–	–	
USi [50]	U_3O_8 (s, 700° C)	–1957.58 ± 12.29	–1007.03 ± 3.08	–43.2 ± 6.2
	–	–	–	
U_3Si_2 [49]	U_3O_8 (s, 700° C)	–5082.26 ± 15.18	–1046.0 ± 3.0	–33.2 ± 3.1
	UO_3 (sln, 700° C)	–5366.20 ± 133.7	–1068.1 ± 26.8	

†Values for a mixture of 0.805 $U_3Si_{5.07}$ – 0.195 o-USi *Value for $U_3Si_{5.07}$ §Determined by combustion calorimetry. ‡Conditions of the measurements are indicated in the parenthesis, *sln* denotes oxide dissolved in sodium molybdate, s indicates solid oxide in oxygen gas atmosphere. Drop calorimetric enthalpies (ΔH_d) correspond to enthalpies of drop solution in sodium molybdate solvent (for UN, U_3Si_2) and transposed temperature drop values in O_2 (for USi, U_3Si_5), all at 700 °C. Enthalpies of oxidation (ΔH_{ox}) correspond to ambient reactions (determined through utilization of appropriate thermochemical cycles) with the final state of UO_3 for UN and U_3Si_2 and of U_3O_8 for USi, U_3Si_5. Standard enthalpies of formation per mol atom ($\Delta H°_f$) are calculated from calorimetric data obtained by high temperature drop calorimetry (for UN, USi, U_3Si_5, U_3Si_2) and other calorimetric techniques (UC).

Figures:

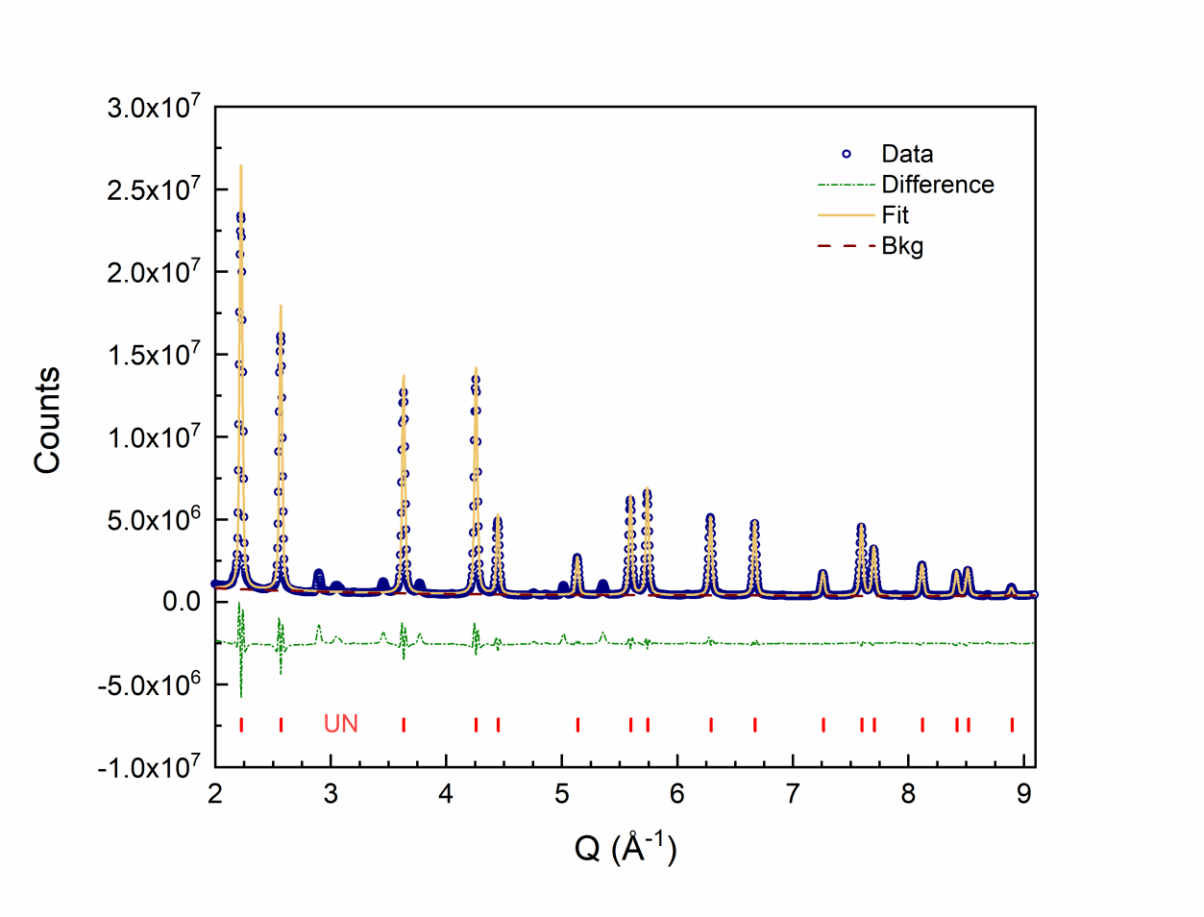

Figure 1. Fitted synchrotron XRD pattern of pristine UN collected at ambient temperature. Data are shown as blue circles and the solid yellow curve is the best fit to the data. The green dashed curve represents the difference between the observed and calculated profiles. The red tick marks above the *x*-axis indicate the positions of allowed diffraction maxima of the UN rock-salt structure. Additional diffraction peaks are identified as α- $UN_{1.5+x}$ no other secondary phases were detected.

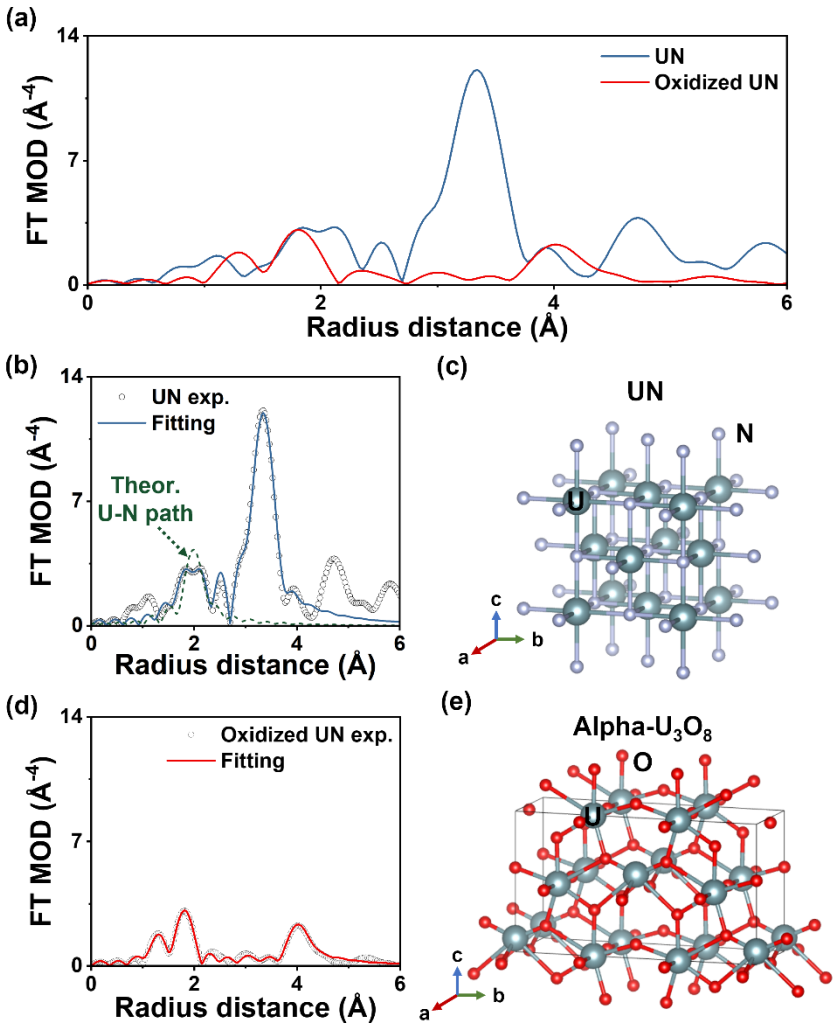

Figure 2. XAFS analysis of pristine UN and oxidized product. (a) radial distribution functions of pristine UN and oxidized phase (U_3O_8). (b) and (c): fitting of pristine UN in the *R* space. (d) and (e): fitting of the oxidized phase using α-U_3O_8 model in the *R* space.

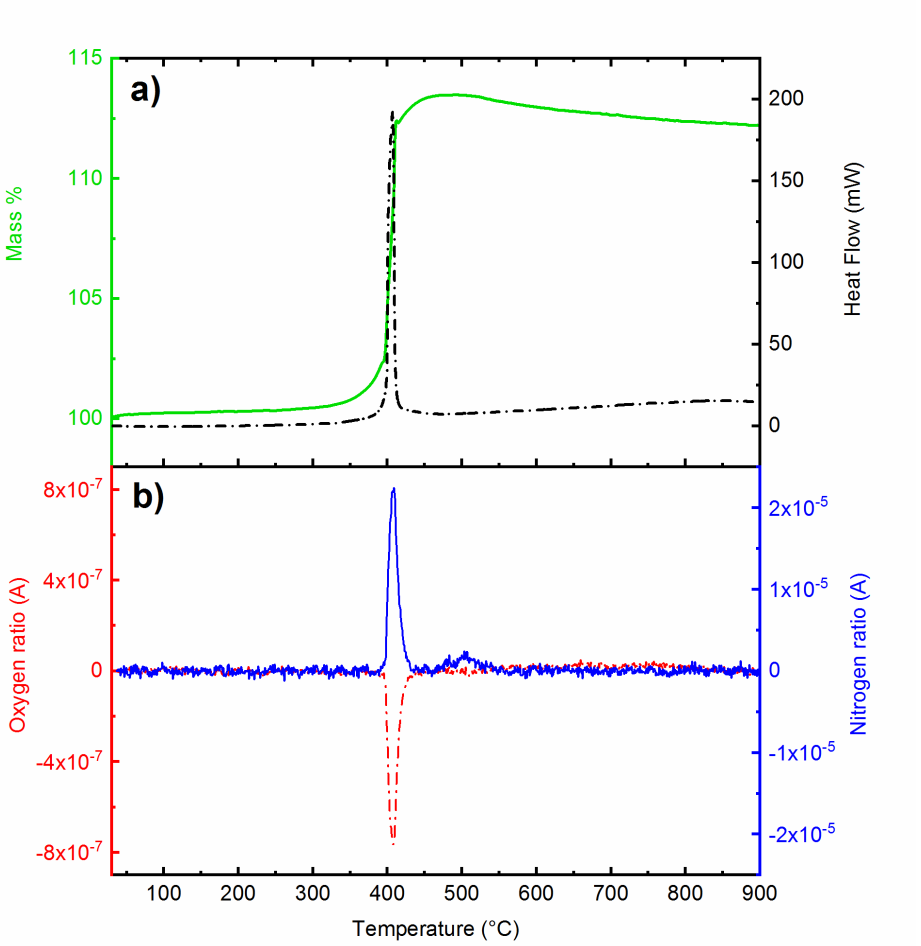

Figure 3. TGA-DSC-MS curves of UN from 25 to 900 ºC in air using a heating rate of 10 ºC/min and an air flow rate of 60 ml/min. (a) The green TG curve represents the change in the mass % of the sample, the dashed black DSC curve indicates the corresponding heat flow with the upward direction being exothermic. (b) The blue MS curve represents the ion current signal of m/z = 28 corresponding to the primary mass ratio of N_2. The red dashed MS curve represents the ion current m/z = 16 corresponding to the mass ratio of O_2.

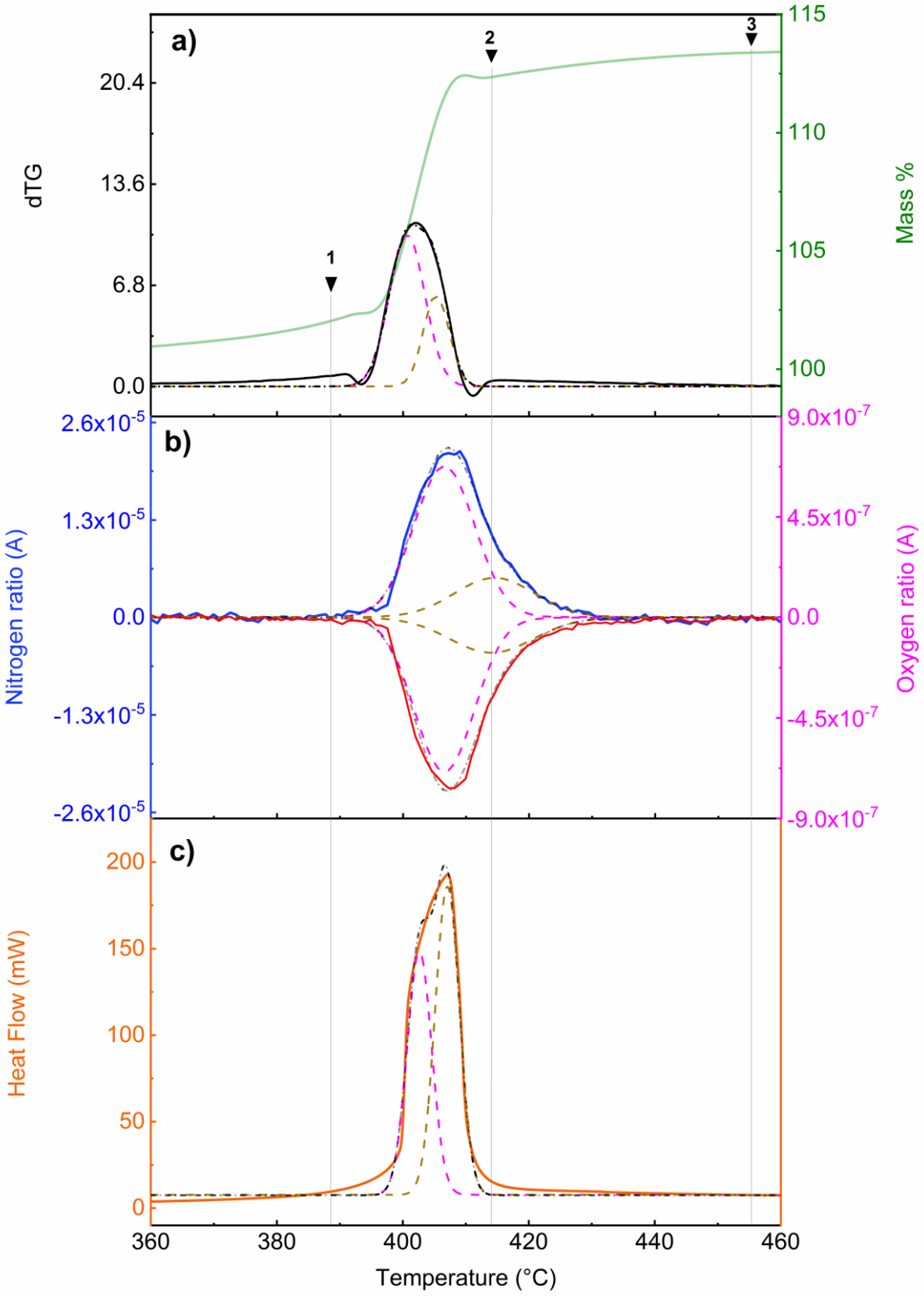
a)
b)
c)
1
2
3
dTG
Mass %
20.4
13.6
6.8
0.0
115
110
105
100
2.6x10-5
1.3x10-5
0.0
-1.3x10-5
-2.6x10-5
9.0x10-7
4.5x10-7
0.0
-4.5x10-7
-9.0x10-7
Nitrogen ratio (A)
Oxygen ratio (A)
Heat Flow (mW)
200
150
100
50
0
360
380
400
420
440
460
Temperature (°C)

Figure 4. TG-MS-DSC profiles of UN from 360 to 460 ºC deconvoluted using two step Gaussian fits (dashed curves) with a general form of $y = y_0 + [A \cdot e^{-(z\cdot((T-\mu)/\sigma)^2}]/[\sigma\cdot\sqrt{(\pi/z)}]$, where T is the corresponding temperature and $z = 4\cdot Ln(2)$. Black dashed curves represent the cumulative distribution from the normal fits. (a) Gaussian deconvolution of the differential of mass change (dTG) with respect to temperature (black); TG mass % curve is from Figure 1 (green). (b) Gaussian deconvolution of the MS signals of released N_2 (blue) and absorbed O_2 (red) gases. (c) Gaussian deconvolution of the DSC heat flow curve (orange). Full description of the deconvolution equations used can be found at the end of the S.I. Indices **1**,**2**,**3** denote the temperatures of interest corresponding to 389, 414, and 464 °C, respectively.

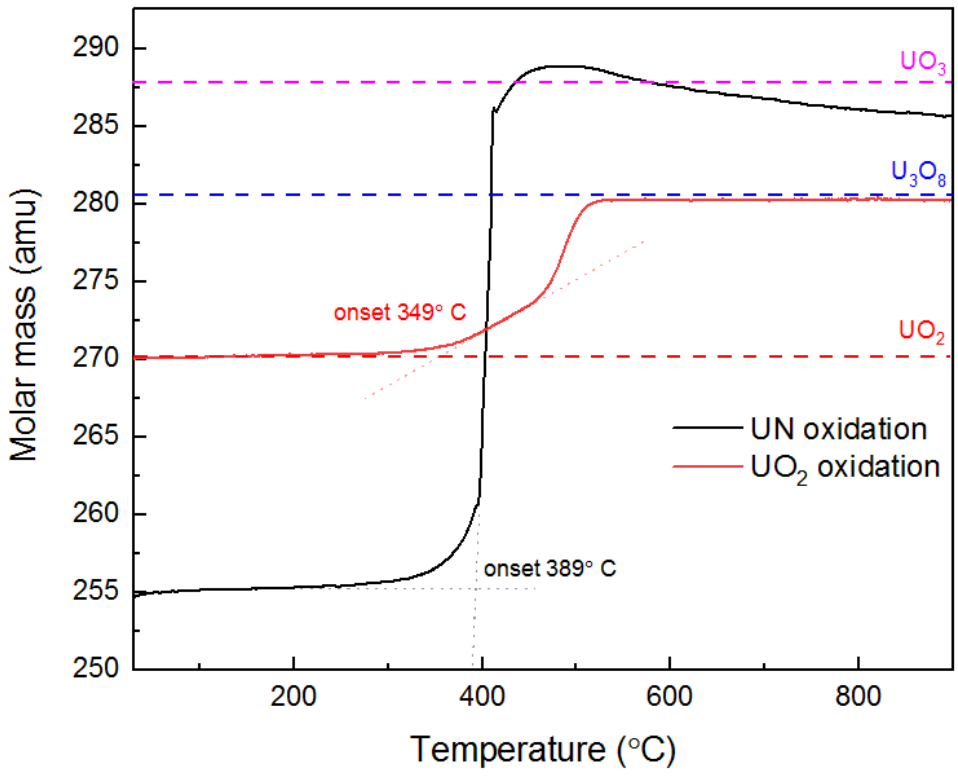

Figure 5. Comparison of TGA profiles between UN (current work) and UO_2 [93] upon oxidation. Black curve represents the experimental mass change of UN with the starting composition of $UN\cdot 0.007UN_{1.5+x}\cdot 0.0035UO_2$ (254.55 g/mol), while red curve represents that of UO_2 [93]. For ease of comparison, the mass change data have been normalized on a basis of per mole of U. Dashed

magenta, blue, and red curves represent the molar masses of UO_3 (286.29 g/mol), $1/3U_3O_8$ (280.70 g/mol) and UO_2 (270.03 g/mol) respectively. The faded dotted lines (red and black corresponding to UO_2 and UN, respectively) represent the tangents of mass change used to calculate the onset bulk oxidation temperatures.

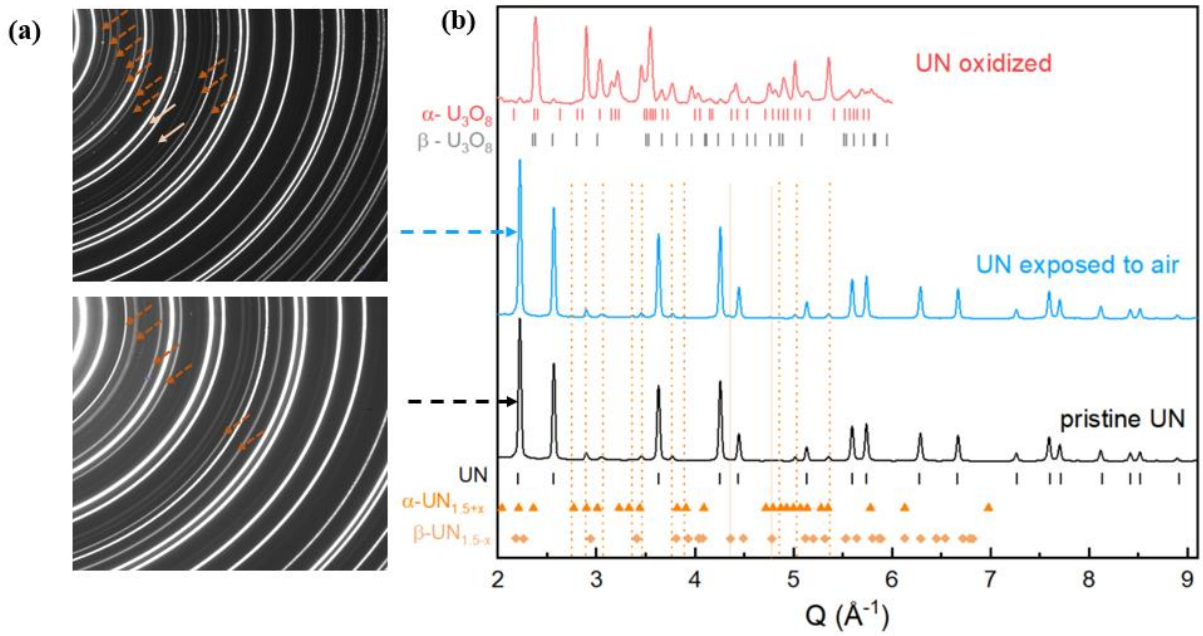

Figure 6. (a) 2D synchrotron diffraction patterns of UN exposed to an ambient atmosphere for 12 hours (left top) and pristine UN (left bottom). Orange dashed arrows indicate the primary diffractions of α-$UN_{1.5+x}$ and solid peach-colored arrows indicate detected diffractions of β-$UN_{1.5-x}$; indexed in the adjacent subfigure by dashed and solid lines respectively. (b) 1D synchrotron diffraction patterns of pristine UN (indexed by black dashes), UN exposed to ambient atmosphere for 12 hours (α-$UN_{1.5+x}$ and β-$UN_{1.5-x}$ indexed by orange triangles and peach-colored diamonds respectively), and UN oxidized in an air atmosphere using a heating rate of 10 °C/min up to 900 °C (simulating TGA conditions in Figure 3) indexed by α-U_3O_8 (light red dashes) and β-U_3O_8 (grey dashes).

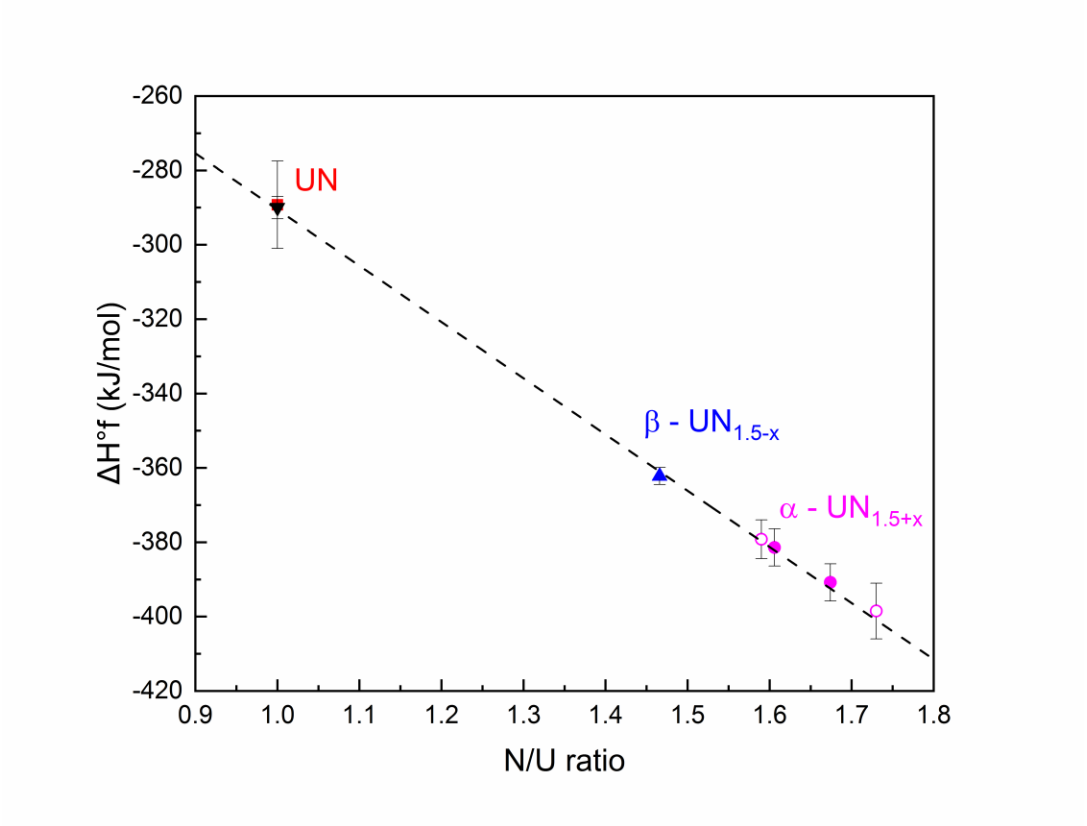

Figure 7. Standard enthalpy of formation of uranium nitrides vs N/U molar ratio. Red square represents the experimental value determined in the current work, black triangle (covering the square) represents the selected enthalpy of formation value for UN from a thermodynamic review [52], based on the weighted average of previous calorimetric studies [51,109],blue triangle and the magenta circles represent values for the β-$UN_{1.5-x}$ and α-$UN_{1.5+x}$, respectively, determined by previous calorimetric methods [52]. Open magenta circles indicate previously extrapolated values for α – $UN_{1.5+x}$ at the corresponding compositions. The data are fitted by $\Delta H°_f$ (kJ/mol) = – (151.2 ± 2.0)·[U/N] – (139.3 ± 2.9) with an adjusted R^2 = 0.9989.

References:

[1] K.A. Terrani, B.C. Jolly, J.M. Harp, Uranium nitride tristructural-isotropic fuel particle, J. Nucl. Mater. 531 (2020) 152034. https://doi.org/10.1016/j.jnucmat.2020.152034.

[2] I. Grenthe, J. Fuger, R.J.M. Konings, R.J. Lemire, A.B. Muller, C. Nguyen-Trung Cregu, H. Wanner, Chemical Thermodynamics of Uranium, 2nd ed., 2003.

[3] I.A. Hassan, A.A. Badawi, A. El Saghir, M.K. Shaat, Viability of uranium nitride (UN) as annular fuel for AP-1000, Prog. Nucl. Energy. 110 (2019) 170–177. https://doi.org/10.1016/j.pnucene.2018.09.020.

[4] X. Guo, X. Lü, J.T. White, C.J. Benmore, A.T. Nelson, R.C. Roback, H. Xu, Bulk moduli and high pressure crystal structure of U3Si2, J. Nucl. Mater. 523 (2019) 135–142. https://doi.org/10.1016/j.jnucmat.2019.06.006.

[5] J.L. Baker, G. Wang, T. Ulrich, J.T. White, E.R. Batista, P. Yang, R.C. Roback, C. Park, H. Xu, High-pressure structural behavior and elastic properties of U3Si5: A combined synchrotron XRD and DFT study, J. Nucl. Mater. 540 (2020) 152373. https://doi.org/10.1016/j.jnucmat.2020.152373.

[6] T.M. Besmann, J.W. McMurrary, A.T. Nelson, J.T. White, E.J. Lahoda, S.C. Middleburgh, A. Claisse, T.L. Ulrich, K.E. Johnson, V. Kocevski, D. Adorno Lopes, S.C. Vogel, Phase Equilibria and Thermochemistry of Advanced Fuels: Modeling Burnup Behavior, Idaho Falls, ID (United States), 2020. https://doi.org/10.2172/1606266.

[7] H.M. Reiche, S.C. Vogel, M. Tang, In situ synthesis and characterization of uranium carbide using high temperature neutron diffraction, J. Nucl. Mater. 471 (2016) 308–316. https://doi.org/10.1016/j.jnucmat.2015.12.044.

[8] R. Ducher, R. Dubourg, M. Barrachin, A. Pasturel, First-principles study of defect behavior in irradiated uranium monocarbide, Phys. Rev. B - Condens. Matter Mater. Phys. 83 (2011) 104107. https://doi.org/10.1103/PhysRevB.83.104107.

[9] O. Fiquet, G. Raveu, G. Martin, P. Garcia, Influence of the sintering atmosphere on dense Uranium mono-carbide properties, 2020. https://hal-cea.archives-ouvertes.fr/cea-02520553 (accessed October 8, 2020).

[10] T.L. Wilson, E.E. Moore, D. Adorno Lopes, V. Kocevski, E. Sooby Wood, J.T. White, A.T. Nelson, J.W. McMurray, S.C. Middleburg, P. Xu, T.M. Besmann, Uranium nitride-silicide advanced nuclear fuel: higher efficiency and greater safety, Adv. Appl. Ceram.

117 (2018) s76–s81. https://doi.org/10.1080/17436753.2018.1521607.

[11] S. Middlemas, Z. Hua, V. Chauhan, W.T. Yorgason, R. Schley, A. Khanolkar, M. Khafizov, D. Hurley, Determining local thermal transport in a composite uranium-nitride/silicide nuclear fuel using square-pulse transient thermoreflectance technique, J. Nucl. Mater. 528 (2020) 151842. https://doi.org/10.1016/j.jnucmat.2019.151842.

[12] B. Szpunar, J.I. Ranasinghe, L. Malakkal, J.A. Szpunar, First principles investigation of thermal transport of uranium mononitride, J. Phys. Chem. Solids. 146 (2020) 109636. https://doi.org/10.1016/j.jpcs.2020.109636.

[13] E.F. Westrum, C.M. Barber, Uranium Mononitride: Heat Capacity and Thermodynamic Properties from 5° to 350 0 K*, 1966.

[14] J.F. Fletcher, J. Greenborg, NITRIDE FUELS FOR FAST BREEDER REACTORS: FUEL CYCLE CONSIDERATIONS., Richland, WA (United States), 1968. https://doi.org/10.2172/4543207.

[15] B. Raj, Core materials, in: Fast Spectr. React., Springer US, 2012: pp. 299–363. https://doi.org/10.1007/978-1-4419-9572-8_11.

[16] J.W. Jeffery, Uranium use in fast reactors [2], Nature. 281 (1979) 98. https://doi.org/10.1038/281098b0.

[17] P.A. Nelson, M.G. Chasanov, URANIUM NITRIDE--SODIUM PASTE FUEL FOR FAST-REACTOR BLANKETS., Argonne, IL (United States), 1968. https://doi.org/10.2172/4831462.

[18] P. Söderlind, A. Landa, A. Perron, B. Sadigh, T.W. Heo, Ground-State and Thermodynamical Properties of Uranium Mononitride from Anharmonic First-Principles Theory, Appl. Sci. 9 (2019) 3914. https://doi.org/10.3390/app9183914.

[19] K. Minato, M. Akabori, M. Takano, Y. Arai, K. Nakajima, A. Itoh, T. Ogawa, Fabrication of nitride fuels for transmutation of minor actinides, in: J. Nucl. Mater., North-Holland, 2003: pp. 18–24. https://doi.org/10.1016/S0022-3115(03)00163-6.

[20] A.T. Nelson, P. Demkowicz, Other power reactor fuels, in: Adv. Nucl. Fuel Chem., Elsevier, 2020: pp. 215–247. https://doi.org/10.1016/b978-0-08-102571-0.00006-9.

[21] M. Streit, F. Ingold, Nitrides as a nuclear fuel option, J. Eur. Ceram. Soc. 25 (2005) 2687–2692. https://doi.org/10.1016/j.jeurceramsoc.2005.03.181.

[22] E. Lawrence Bright, S. Rennie, A. Siberry, K. Samani, K. Clarke, D.T. Goddard, R.

Springell, Comparing the corrosion of uranium nitride and uranium dioxide surfaces with H 2 O 2, J. Nucl. Mater. 518 (2019) 202–207. https://doi.org/10.1016/j.jnucmat.2019.03.006.

[23] C.H. Johnson, H.H. Barschall, Interaction of Fast Neutrons with Nitrogen, Phys. Rev. 80 (1950) 818. https://doi.org/10.1103/PhysRev.80.818.

[24] V.M. Troyanov, A.F. Grachev, L.M. Zabud'ko, M. V. Skupov, Prospects for Using Nitride Fuel in Fast Reactors with a Closed Nuclear Fuel Cycle, At. Energy. 117 (2014) 85–91. https://doi.org/10.1007/s10512-014-9893-1.

[25] V.I. Matveev, I.V. Malysheva, I.V. Buriyevskiy, Physical characteristics of large fast-neutron sodium-cooled reactors with advanced nitride and metallic fuels, Nucl. Energy Technol. 1 (2015) 308–312. https://doi.org/10.1016/j.nucet.2016.02.021.

[26] B.D. Rogozkin, N.M. Stepennova, A.A. Proshkin, Mononitride Fuel for Fast Reactors, At. Energy 2003 953. 95 (2003) 624–636. https://doi.org/10.1023/B:ATEN.0000007886.86817.32.

[27] B. RAJ, M. L, P. RAO, M.D. MATHEW, Development of fuels and structural materials for fast breeder reactors, Sadhana. 27 (2002) 527–558.

[28] T.B. Cochran, H.A. Feiveson, W. Patterson, G. Pshakin, M. V Ramana, M. Schneider, T. Suzuki, F. Von Hippel, Fast Breeder Reactor Programs: History and Status, 2010. www.fissilematerials.org (accessed October 8, 2020).

[29] A.E. Waltar, D.R. Todd, P. V. Tsvetkov, Fast spectrum reactors, Springer US, 2012. https://doi.org/10.1007/978-1-4419-9572-8.

[30] N.K. Sinha, B. Raj, Development of polymeric applications for sodium cooled Fast Breeder Reactors: Chronicles of inception, progress and achievements, in: Nucl. Eng. Des., North-Holland, 2010: pp. 2925–2947. https://doi.org/10.1016/j.nucengdes.2010.07.028.

[31] G. Locatelli, M. Mancini, N. Todeschini, Generation IV nuclear reactors: Current status and future prospects, Energy Policy. 61 (2013) 1503–1520. https://doi.org/10.1016/j.enpol.2013.06.101.

[32] I.L. Pioro, Handbook of Generation IV Nuclear Reactors, Handb. Gener. IV Nucl. React. (2016) 1–911. https://doi.org/10.1016/C2014-0-01699-1.

[33] D.S. Tucker, CERMETS for Use in Nuclear Thermal Propulsion, Adv. Compos. Mater.

Dev. (2019). https://doi.org/10.5772/INTECHOPEN.85220.

[34] R.R. Hickman, J.W. Broadway, O.R. Mireles, Fabrication and Testing of CERMET Fuel Materials for Nuclear Thermal Propulsion, (n.d.).

[35] A.M. Raftery, R.L. Seibert, D.R. Brown, M.P. Trammell, A.T. Nelson, K.A. Terrani, Fabrication of UN-Mo CERMET Nuclear Fuel Using Advanced Manufacturing Techniques, Https://Doi.Org/10.1080/00295450.2020.1823187. 207 (2020) 815–824. https://doi.org/10.1080/00295450.2020.1823187.

[36] D. Zhang, Generation IV concepts: China, in: Handb. Gener. IV Nucl. React., Elsevier Inc., 2016: pp. 373–411. https://doi.org/10.1016/B978-0-08-100149-3.00014-8.

[37] P. Tsvetkov, A. Waltar, D. Todd, Sustainable development of nuclear energy and the role of fast spectrum reactors, in: Fast Spectr. React., Springer US, 2012: pp. 3–22. https://doi.org/10.1007/978-1-4419-9572-8_1.

[38] P. Yvon, Structural materials for Generation IV nuclear reactors, Elsevier Inc., 2016. https://doi.org/10.1016/c2014-0-03589-7.

[39] M. Paljević, Z. Despotović, Oxidation of uranium mononitride, J. Nucl. Mater. 57 (1975) 253–257. https://doi.org/10.1016/0022-3115(75)90208-1.

[40] M. Jolkkonen, P. Malkki, K. Johnson, J. Wallenius, Uranium nitride fuels in superheated steam, J. Nucl. Sci. Technol. 54 (2017) 513–519. https://doi.org/10.1080/00223131.2017.1291372.

[41] E.F.J. Westrum, C.M. Barber, Uranium Mononitride: Heat Capacity and Thermodynamic Properties from 5° to 350°K, J. Chem. Phys. 45 (1966).

[42] C. Affortit, Chaleur specifique de UC et UN, J. Nucl. Mater. 34 (1970) 105–107. https://doi.org/10.1016/0022-3115(70)90014-0.

[43] V.V. Akhachinskij, S.N. Bashlykov, Thermodynamics of the uranium-carbon-, uranium-nitrogen- and plutonium-carbon systems, At. Energ. 29 (1970) 439–447. http://inis.iaea.org/Search/search.aspx?orig_q=RN:2006552 (accessed July 17, 2020).

[44] S.L. Hayes, J.K. Thomas, K.L. Peddicord, Material property correlations for uranium mononitride. I. Physical properties, J. Nucl. Mater. 171 (1990) 262–270. https://doi.org/10.1016/0022-3115(90)90374-V.

[45] T. Matsui, R.W. Ohse, Thermodynamic properties of uranium nitride, plutonium nitride and uranium-plutonium mixed nitride, High Temp. - High Press. 19 (1987) 1–17.

[46] R.M. Dell, V.J. Wheeler, E.J. Mciver, Oxidation of uranium mononitride and uranium monocarbide, Trans. Faraday Soc. 62 (1966) 3591–3606. https://doi.org/10.1039/tf9666203591.

[47] L. Lu, F. Li, Y. Hu, H. Xiao, B. Bai, Y. Zhang, L. Luo, J. Liu, K. Liu, The initial oxidation behaviors of uranium nitride UNx (x = 0, 0.23, 0.68, 1.66) films, J. Nucl. Mater. 480 (2016) 189–194. https://doi.org/10.1016/j.jnucmat.2016.08.025.

[48] S.A. Kulyukhin, Y.M. Nevolin, V.G. Petrov, S.N. Kalmykov, Volume oxidation of uranium mononitride and uranium monocarbide in the dry NOX-gaseous atmosphere, Radiochim. Acta. 1 (2020) aop. https://doi.org/10.1515/ract-2019-3125.

[49] X. Guo, J.T. White, A.T. Nelson, A. Migdisov, R. Roback, H. Xu, Enthalpy of formation of U3Si2: A high-temperature drop calorimetry study, J. Nucl. Mater. 507 (2018) 44–49. https://doi.org/10.1016/j.jnucmat.2018.04.032.

[50] C.K. Chung, X. Guo, G. Wang, T.L. Wilson, J.T. White, A.T. Nelson, A. Shelyug, H. Boukhalfa, P. Yang, E.R. Batista, A.A. Migdisov, R.C. Roback, A. Navrotsky, H. Xu, Enthalpies of formation and phase stability relations of USi, U3Si5 and U3Si2, J. Nucl. Mater. 523 (2019) 101–110. https://doi.org/10.1016/j.jnucmat.2019.05.052.

[51] G.K. Johnson, E.H.P. Cordfunke, The enthalpies of formation of uranium mononitride and α- and β-uranium sesquinitride by fluorine bomb calorimetry, J. Chem. Thermodyn. 13 (1981) 273–282. https://doi.org/10.1016/0021-9614(81)90127-0.

[52] I. Grenthe, J. Fuger, R.J.M. Konings, R.J. Lemire, A.B. Muller, H. Wanner, I. Forest, CHEMICAL THERMODYNAMICS OF URANIUM, 2004. http://www.copyright.com/. (accessed September 7, 2020).

[53] Y. Arai, 3.02 - Nitride Fuel A2 - Konings, Rudy J.M, in Comprehensive Nuclear Materials., in: R.J.M. Konings (Ed.), Compr. Nucl. Mater., Elsevier: Oxford, 2012: pp. 41–54.

[54] C. Prescher, V.B. Prakapenka, DIOPTAS: A Program for Reduction of Two-Dimensional X-Ray Diffraction Data and Data Exploration, High Press. Res. 35 (2015) 233–230.

[55] B.H. Toby, R.B. Von Dreele, GSAS-II: The genesis of a modern open-source all purpose crystallography software package, J. Appl. Crystallogr. 46 (2013) 544–549. https://doi.org/10.1107/S0021889813003531.

[56] H. Xu, X. Guo, J. Bai, Thermal behavior of polyhalite: a high-temperature synchrotron

XRD study, Phys. Chem. Miner. 44 (2017) 125–135. https://doi.org/10.1007/s00269-016-0842-5.

[57] X. Guo, X. Lü, J.T. White, C.J. Benmore, A.T. Nelson, R.C. Roback, H. Xu, Bulk moduli and high pressure crystal structure of U_3Si_2, J. Nucl. Mater. 523 (2019) 135–142. https://doi.org/10.1016/j.jnucmat.2019.06.006.

[58] A.C. Strzelecki, K. Kriegsman, P. Estevenon, V. Goncharov, J. Bai, S. Szenknect, A. Mesbah, D. Wu, J.S. Mccloy, N. Dacheux, X. Guo, High-Temperature Thermodynamics of Cerium Silicates, A-Ce2Si2O7, and Ce4.67(SiO4)3O, ACS Earth Sp. Chem. 4 (2020) 2129–2143. https://doi.org/10.1021/ACSEARTHSPACECHEM.0C00231.

[59] A.C. Strzelecki, T. Barral, P. Estevenon, A. Mesbah, V. Goncharov, J. Baker, J. Bai, N. Clavier, S. Szenknect, A. Migdissov, H. Xu, R.C. Ewing, N. Dacheux, X. Guo, The Role of Water and Hydroxyl Groups in the Structures of Stetindite and Coffinite, MSiO4 (M = Ce, U), Inorg. Chem. (2021). https://doi.org/10.1021/acs.inorgchem.0c02757.

[60] B. Ravel, M. Newville, ATHENA, ARTEMIS, HEPHAESTUS: Data analysis for X-ray absorption spectroscopy using IFEFFIT, J. Synchrotron Radiat. 12 (2005) 537–541. https://doi.org/10.1107/S0909049505012719.

[61] E. Enriquez, G. Wang, Y. Sharma, I. Sarpkaya, Q. Wang, D. Chen, N. Winner, X. Guo, J. Dunwoody, J. White, A. Nelson, H. Xu, P. Dowden, E. Batista, H. Htoon, P. Yang, Q. Jia, A. Chen, Structural and Optical Properties of Phase-Pure UO 2 , α-U 3 O 8 , and α-UO 3 Epitaxial Thin Films Grown by Pulsed Laser Deposition, Cite This ACS Appl. Mater. Interfaces. 12 (2020) 35241. https://doi.org/10.1021/acsami.0c08635.

[62] A. Claisse, M. Klipfel, N. Lindbom, M. Freyss, P. Olsson, GGA+U study of uranium mononitride: A comparison of the U-ramping and occupation matrix schemes and incorporation energies of fission products, J. Nucl. Mater. 478 (2016) 119–124. https://doi.org/10.1016/J.JNUCMAT.2016.06.007.

[63] J.J. Rehr, R.C. Albers, S.I. Zabinsky, High-order multiple-scattering calculations of x-ray-absorption fine structure, Phys. Rev. Lett. 69 (1992) 3397. https://doi.org/10.1103/PhysRevLett.69.3397.

[64] B. Ravel, Path degeneracy and EXAFS analysis of disordered materials, J. Synchrotron Radiat. 21 (2014) 1269–1274.

[65] X. Guo, S. V. Ushakov, S. Labs, H. Curtius, D. Bosbach, A. Navrotsky, Energetics of

metastudtite and implications for nuclear waste alteration, Proc. Natl. Acad. Sci. U. S. A. 111 (2014) 17737–17742. https://doi.org/10.1073/pnas.1421144111.

[66] A.C. Strzelecki, K. Kriegsman, P. Estevenon, V. Goncharov, J. Bai, S. Szenknect, A. Mesbah, D. Wu, J.S. McCloy, N. Dacheux, X. Guo, High-Temperature Thermodynamics of Cerium Silicates, A-Ce 2 Si 2 O 7 , and Ce 4.67 (SiO 4) 3 O , ACS Earth Sp. Chem. (2020). https://doi.org/10.1021/acsearthspacechem.0c00231.

[67] A. Navrotsky, Progress and New Directions in Calorimetry: A 2014 Perspective, J. Am. Ceram. Soc. 97 (2014) 3349–3359. https://doi.org/10.1111/jace.13278.

[68] X. Guo, H. Boukhalfa, J.N. Mitchell, M. Ramos, A.J. Gaunt, A. Migliori, R.C. Roback, A. Navrotsky, H. Xu, Sample seal-and-drop device and methodology for high temperature oxide melt solution calorimetric measurements of PuO2, Rev. Sci. Instrum. 90 (2019) 044101. https://doi.org/10.1063/1.5093567.

[69] X. Guo, S. Szenknect, A. Mesbah, S. Labs, N. Clavier, C. Poinssot, S. V. Ushakov, H. Curtius, D. Bosbach, R.C. Ewing, P.C. Burns, N. Dacheux, A. Navrotsky, Thermodynamics of formation of coffinite, USiO4, Proc. Natl. Acad. Sci. U. S. A. 112 (2015) 6551–6555. https://doi.org/10.1073/pnas.1507441112.

[70] K.B. Helean, A. Navrotsky, E.R. Vance, M.L. Carter, B. Ebbinghaus, O. Krikorian, J. Lian, L.M. Wang, J.G. Catalano, Enthalpies of formation of Ce-pyrochlore, J. Nucl. Mater. 303 (2002) 226–239. https://doi.org/10.1016/S0022-3115(02)00795-X.

[71] X. Guo, E. Tiferet, L. Qi, J.M. Solomon, A. Lanzirotti, M. Newville, M.H. Engelhard, R.K. Kukkadapu, D. Wu, E.S. Ilton, M. Asta, S.R. Sutton, H. Xu, A. Navrotsky, U(v) in metal uranates: A combined experimental and theoretical study of MgUO4, CrUO4, and FeUO4, Dalt. Trans. 45 (2016) 4622–4632. https://doi.org/10.1039/c6dt00066e.

[72] X. Guo, D. Wu, H. Xu, P.C. Burns, A. Navrotsky, Thermodynamic studies of studtite thermal decomposition pathways via amorphous intermediates UO3, U2O7, and UO4, J. Nucl. Mater. 478 (2016) 158–163. https://doi.org/10.1016/j.jnucmat.2016.06.014.

[73] X. Guo, P. Szenknect, A. Mesbah, N. Clavier, C. Poinssot, D. Wu, H. Xu, N. Dacheux, R.C. Ewing, A. Navrotsky, Energetics of a Uranothorite (Th 1−x U x SiO 4) Solid Solution, Chem. Mater. 28 (2016) 7117–7124. https://doi.org/10.1021/acs.chemmater.6b03346.

[74] † M. R. Ranade, †,‡ F. Tessier, *,† A. Navrotsky, † V. J. Leppert, † S. H. Risbud, ‡

and F. J. DiSalvo, C.M. Balkas§, Enthalpy of Formation of Gallium Nitride, J. Phys. Chem. B. 104 (2000) 4060–4063. https://doi.org/10.1021/JP993752S.

[75] F. Tessier, A. Navrotsky, R. Niewa, A. Leineweber, H. Jacobs, S. Kikkawa, M. Takahashi, F. Kanamaru, F.J. DiSalvo, Energetics of binary iron nitrides, Solid State Sci. 2 (2000) 457–462. https://doi.org/10.1016/S1293-2558(00)00151-5.

[76] F. Tessier, M.R. Ranade, A. Navrotsky, R. Niewa, F.J. Disalvo, A. Leineweber, H. Jacobs, Thermodynamics of Formation of Binary and Ternary Nitrides in the System Ce/Mn/N, Zeitschrift Fur Anorgannische Und Allgmeine Chemie. 627 (2001) 194–200. https://doi.org/10.1002/1521-3749.

[77] A.A. Voskanyan, A.A. Voskanyan, V.G. Goncharov, N. Novendra, X. Guo, A. Navrotsky, A. Navrotsky, Thermodynamics Drives the Stability of the MOF-74 Family in Water, ACS Omega. 5 (2020) 13158–13163. https://doi.org/10.1021/acsomega.0c01189.

[78] L. He, M. Khafizov, C. Jiang, B. Tyburska-Püschel, B.J. Jaques, P. Xiu, P. Xu, M.K. Meyer, K. Sridharan, D.P. Butt, J. Gan, Phase and defect evolution in uranium-nitrogen-oxygen system under irradiation, Acta Mater. 208 (2021) 116778. https://doi.org/10.1016/J.ACTAMAT.2021.116778.

[79] Y. Suzuki, Y. Arai, Thermophysical and thermodynamic properties of actinide mononitrides and their solid solutions, J. Alloys Compd. 271–273 (1998) 577–582. https://doi.org/10.1016/S0925-8388(98)00160-1.

[80] M.S. Chinthaka, D.H. Rodney, L.S. Lance, A.T. Kurt, Synthesis of Phase-Pure U2N3 Microspheres and Its Decomposition into UN, Inorg. Chem. 54 (2015) 293–298.

[81] J. Chen, Z. Long, R. Qiu, Y. Hu, B. Ao, K. Liu, Molecular reactions and oxidation corrosion on UN (001) surface under exposure to environment gases: A DFT study, J. Nucl. Mater. 533 (2020) 152095. https://doi.org/10.1016/j.jnucmat.2020.152095.

[82] S.D. Conradson, D. Manara, F. Wastin, D.L. Clark, G.H. Lander, L.A. Morales, J. Rebizant, V. V Rondinella, Local Structure and Charge Distribution in the UO2−U4O9 System, Inorg. Chem. 43 (2004) 6922–6935.

[83] S.D. Conradson, T. Durakiewicz, F.J. Espinosa-Faller, Y.Q. An, D.A. Andersson, A.R. Bishop, K.S. Boland, J.A. Bradley, D.D. Byler, D.L. Clark, D.R. Conradson, L.L. Conradson, A.L. Costello, N.J. Hess, G.H. Lander, A. Llobet, M.B. Martucci, J. Mustre De Leon, D. Nordlund, J.S. Lezama-Pacheco, T.E. Proffen, G. Rodriguez, D.E. Schwarz,

G.T. Seidler, A.J. Taylor, S.A. Trugman, T.A. Tyson, J.A. Valdez, Possible Bose-condensate behavior in a quantum phase originating in a collective excitation in the chemically and optically doped Mott-Hubbard system UO 2+x, Phys. Rev. B. 88 (2013) 115135. https://doi.org/10.1103/PhysRevB.88.115135.

[84] J. Qin, X. Wang, Y. Zhang, Y. Hu, L. Lu, P. Zhou, F. Li, Y. Zhang, K. Liu, M. Shuai, Oxidation kinetics of uranium treated by pulsed laser nitriding in air, Surf. Coatings Technol. 357 (2019) 864–869. https://doi.org/10.1016/j.surfcoat.2018.10.093.

[85] Z. Long, R. Zeng, Y. Hu, J. Liu, W. Wang, Y. Zhao, Z. Luo, B. Bai, X. Wang, K. Liu, Electronic structure and fine structural features of the air-grown UN x O y on nitrogen-rich uranium nitride, Appl. Surf. Sci. 443 (2018) 407–411. https://doi.org/10.1016/j.apsusc.2018.02.271.

[86] R. M. Dell, V. J. Wheeler, E. J. McIver, Oxidation of uranium mononitride and uranium monocarbide, Trans. Faraday Soc. 62 (1966) 3591–3606. https://doi.org/10.1039/TF9666203591.

[87] Y. Miao, K. Mo, T. Yao, J. Lian, J. Fortner, L. Jamison, R. Xu, A.M. Yacout, Correlation between crystallographic orientation and surface faceting in UO2, J. Nucl. Mater. 478 (2016) 176–184. https://doi.org/10.1016/j.jnucmat.2016.05.044.

[88] C. Kempter, J. McGuire, M.R. Ndler, Uranium Mononitride- Crystolographic Data, Anal. Chem. 177 (1959) 156.

[89] L.G. Gonzalez Fonseca, M. Hedberg, L. Huan, P. Olsson, T. Retegan Vollmer, Application of SPS in the fabrication of UN and (U,Th)N pellets from microspheres, J. Nucl. Mater. 536 (2020) 152181. https://doi.org/10.1016/j.jnucmat.2020.152181.

[90] J. V. Dehadraya, S.K. Mukerjee, G.A. Rama Rao, V.N. Vaidya, V. Venugopal, D.D. Sood, The oxidation of uranium-cerium mononitride microspheres, J. Alloys Compd. 257 (1997) 313–321. https://doi.org/10.1016/S0925-8388(97)00010-8.

[91] S.M. Thein, P.J. Bereolos, Thermal Stabilization of 233 UO 2 , 233 UO 3 , and 233 U 3 O 8, n.d.

[92] V.J. Wheeler, R.M. Dell, E. Wait, Uranium trioxide and the UO3 hydrates, J. Inorg. Nucl. Chem. 26 (1964) 1829–1845. https://doi.org/10.1016/0022-1902(64)80007-5.

[93] T.A. Olds, S.E. Karcher, K.W. Kriegsman, X. Guo, J.S. McCloy, Oxidation and anion lattice defect signatures of hypostoichiometric lanthanide-doped UO2, J. Nucl. Mater. 530

(2020) 151959. https://doi.org/10.1016/j.jnucmat.2019.151959.

[94] A. Miskowiec, J.L. Niedziela, T.L. Spano, M.W. Ambrogio, S. Finkeldei, R. Hunt, A.E. Shields, Additional complexity in the Raman spectra of U3O8, J. Nucl. Mater. 527 (2019). https://doi.org/10.1016/J.JNUCMAT.2019.151790.

[95] A.L. Tamasi, K.S. Boland, K. Czerwinski, J.K. Ellis, S.A. Kozimor, R.L. Martin, A.L. Pugmire, D. Reilly, B.L. Scott, A.D. Sutton, G.L. Wagner, J.R. Walensky, M.P. Wilkerson, Oxidation and Hydration of U 3 O 8 Materials Following Controlled Exposure to Temperature and Humidity, Anal. Chem. 87 (2015) 4210–4217. https://doi.org/10.1021/ac504105t.

[96] J.W. Choi, R.J. McEachern, P. Taylor, D.D. Wood, The effect of fission products on the rate of U3O8 formation in SIMFUEL oxidized in air at 250°C, J. Nucl. Mater. 230 (1996) 250–258. https://doi.org/10.1016/0022-3115(96)80022-5.

[97] F.L. Oetting, J.M. Leitnaker, The chemical thermodynamic properties of nuclear materials I. Uranium mononitride, J. Chem. Thermodyn. 4 (1972) 199–211. https://doi.org/10.1016/0021-9614(72)90057-2.

[98] D. Zhou, J. Yu, C. Pu, Y. Song, Prediction of Stable Ground-State Uranium Nitrides at Ambient and High Pressures, ArXiv. (2018). http://arxiv.org/abs/1804.00095 (accessed April 13, 2021).

[99] E.A. Kotomin, R.W. Grimes, Y. Mastrikov, al -, M.A. Korneva, S. V Starikov -, K.B. Joshi, U. Paliwal -, R.A. Evarestov -, Electronic structure of crystalline uranium nitrides UN, U 2 N 3 and UN 2 : LCAO calculations with the basis set optimization Related content Atomic scale DFT simulations of point defects in uranium nitride Atomistic simulation of a superionic transition in fluorite type structures UO Pressure dependent electronic properties of-Be Recent citations, J. Phys. Conf. Ser. OPEN ACCESS. (n.d.). https://doi.org/10.1088/1742-6596/117/1/012015.

[100] E.K. Storms, E.J. Huber, The heat of formation of uranium carbide, J. Nucl. Mater. 23 (1967) 19–24. https://doi.org/10.1016/0022-3115(67)90126-2.

[101] K.D. Johnson, A.M. Raftery, D.A. Lopes, J. Wallenius, Fabrication and microstructural analysis of UN-U3Si2 composites for accident tolerant fuel applications, J. Nucl. Mater. 477 (2016) 18–23. https://doi.org/10.1016/j.jnucmat.2016.05.004.

[102] G.S. Was, D. Petti, S. Ukai, S. Zinkle, Materials for future nuclear energy systems, J.

Nucl. Mater. 527 (2019) 151837. https://doi.org/10.1016/j.jnucmat.2019.151837.

[103] L.H. Ortega, B.J. Blamer, J.A. Evans, S.M. McDeavitt, Development of an accident-tolerant fuel composite from uranium mononitride (UN) and uranium sesquisilicide (U3 Si2) with increased uranium loading, J. Nucl. Mater. 471 (2016) 116–121. https://doi.org/10.1016/j.jnucmat.2016.01.014.

[104] S. Yeo, E. McKenna, R. Baney, G. Subhash, J. Tulenko, Enhanced thermal conductivity of uranium dioxide-silicon carbide composite fuel pellets prepared by Spark Plasma Sintering (SPS), J. Nucl. Mater. 433 (2013) 66–73. https://doi.org/10.1016/j.jnucmat.2012.09.015.

[105] O. Dorofeeva, V.P. Novikov, D.B. Neumann, NIST-JANAF thermochemical tables. I. Ten organic molecules related to atmospheric chemistry, J. Phys. Chem. Ref. Data. 30 (2001) 475–509. https://doi.org/10.1063/1.1364518.

[106] F. Tessier, A. Navrotsky, R. Niewa, A. Leineweber, H. Jacobs, S. Kikkawa, M. Takahashi, F. Kanamaru, F.J. DiSalvo, Energetics of binary iron nitrides, Solid State Sci. 2 (2000) 457–462. https://doi.org/10.1016/S1293-2558(00)00151-5.

[107] B. Dorado, G. Jomard, M. Freyss, M. Bertolus, Stability of oxygen point defects in UO2 by first-principles DFT+U calculations: Occupation matrix control and Jahn-Teller distortion, Phys. Rev. B - Condens. Matter Mater. Phys. 82 (2010) 035114. https://doi.org/10.1103/PhysRevB.82.035114.

[108] R. Robie, B.S. Hemingway, Thermodynamic properties of minerals and related substances at 298.15 K and 1 bar (10^5 pascals) pressure and at higher temperatures, 1995. https://doi.org/10.3133/b2131.

[109] P. Gross, C. Hayman, H. Clayton, Heats of formation of uranium silicides and nitrides, in: Thermodyn. Nucl. Mater., 1962: pp. 653–665.